

Continuous Estimation of Cardiac Output and Arterial
Resistance from Arterial Blood Pressure using a
Third-Order Windkessel Model

by

Said Elias Francis

Bachelor of Science in Electrical Engineering and Computer Science
Massachusetts Institute of Technology (2006)

Submitted to the Department of Electrical Engineering and Computer Science
in partial fulfillment of the requirements for the degree of

Master of Engineering

at the

MASSACHUSETTS INSTITUTE OF TECHNOLOGY

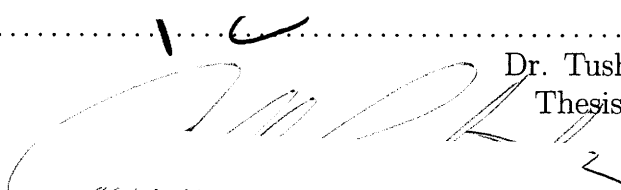
June 2007

© Said Elias Francis, MMVII. All rights reserved.

The author hereby grants to MIT permission to reproduce and distribute publicly
paper and electronic copies of this thesis document in whole or in part.

Author 
Department of Electrical Engineering and Computer Science
May 28, 2007

Certified by 
Professor George C. Verghese
Professor of Electrical Engineering
Thesis Supervisor

Certified by 
Dr. Tushar Parlikar
Thesis Supervisor

Accepted by 
Professor Arthur C. Smith
Chairman, Department Committee on Graduate Students

MASSACHUSETTS INSTITUTE
OF TECHNOLOGY

OCT 03 2007

LIBRARIES

ARCHIVES

Continuous Estimation of Cardiac Output and Arterial Resistance from Arterial Blood Pressure using a Third-Order Windkessel Model

by

Said Elias Francis

Submitted to the Department of Electrical Engineering and Computer Science
on May 28, 2007, in partial fulfillment of the
requirements for the degree of
Master of Engineering

Abstract

Intensive Care Units (ICUs) have high impact on the survival of critically-ill patients in hospitals. Recent statistics have shown that only 10% of the 5 million patients admitted to ICUs in the United States die each year. In modern ICUs, the heart's electrical and mechanical activity is routinely monitored using various sensors. Arterial blood pressure (ABP) and heart rate (HR) are the most commonly recorded waveforms which provide key information to the ICU clinical staff. However, clinicians find themselves in many cases unable to determine the causes behind abnormal behavior of the cardiovascular system because they lack frequent measures of cardiac output (CO), the average blood flow out of the left ventricle. CO is monitored via intermittent thermodilution measurements which are highly invasive and only applied to the sickest ICU patients.

The lack of frequent CO measurements has encouraged researchers to develop estimation methods for cardiac output from routinely measured arterial blood pressure waveforms. The prospects of estimating cardiac output from minimally-invasive blood pressure measurements has resulted in numerous estimation algorithms, however, there is no consensus on the performance of the algorithms that have been proposed.

In this thesis, we investigate the use of a third-order variation of the Windkessel model, which is referred to as the *modified Windkessel model*. We validate its ability to generate well-behaved proximal and distal pressure waveforms for a given flow waveform and thus characterize the arterial tree. We also develop a model-based CO estimation algorithm which uses central and peripheral blood pressure waveforms to obtain reliable estimates of CO and the total peripheral resistance (TPR).

We applied the estimation algorithm to a porcine data set. The results of our estimation algorithm are promising: the weighted-mean root-mean-squared-normalized-error (RMSNE) is about 13.8% over four porcine records. In each porcine experiment, intravenous drug infusions were used to vary CO, ABP, and HR over wide ranges. Our results suggest that the modified Windkessel model is a good representation of the arterial tree and that the estimation algorithm yields reliable estimates of CO and TPR under various hemodynamic conditions.

Thesis Supervisor: Professor George C. Verghese
Title: Professor of Electrical Engineering

Thesis Supervisor: Dr. Tushar Parlikar

Acknowledgments

I would like to take this opportunity to express my deepest gratitude to Professor George Verghese for embracing me with his insightful academic advice for the last five years and for giving me a chance to work under his supervision while pursuing my master's degree. Every Friday, in the conference room of LEES, I would continually be exposed to innovative and modern tools that enhanced my scientific acumen and research ability. I could not have made it through this process without his continued guidance and support.

As for Dr. Thomas Heldt, whose scientific knowledge surpasses anyone's expectations, I can't help exclaiming how inspired I was by him. He has contributed tremendously to my thesis through his rigorous approach to research and refined technical writing. Not only is he an expert in physiological modeling, but also an extremely patient proof-reading ruler. For this, I thank you.

This work would not have been possible if it weren't for Dr. Tushar Parlkar's supervision and friendship. Tushar always found time to discuss my thesis, expanding my scope of knowledge and providing helpful feedback. It was his ability to judge the prospects of any effort that made my research what it is today. I was always stunned by his ability to overcome challenges and excel in all fields, yet maintaining a delightful sense of humor. Kudos to the IHop late night study breaks, which were always accompanied by the most random conversations.

And to Faisal Kashif, my "thank yous" are for helping me overcome the last obstacles in my research. His curiosity and his endless strive for knowledge are admirable qualities, ones which make him stand out in the research community. It's only a matter of time until we hear about the achievements of Dr. Kashif. It is great to see that Faisal teamed up with George to embark on a new journey in modeling which will definitely be of high impact.

Many thanks to Shirley Li, Adam Eisenman, Stavros Valavanis, Gireeja Ranade, and Michael Scharfstein for making the graduate school process so manageable. I am fortunate to have you all around. Special thanks to Shirley for her efforts to bring the members of our research group closer. Thank you Stavros for your true friendship over the years, and for your academic and research collaboration.

To Hashem Dabbas, who was there for me in hardships, always pushing me to strive for the best, I extend my great appreciation. I am looking forward to our post-MIT experience in New York, and I feel relieved that I have someone I can count on during the next two years.

How can I not mention Hadi Zaklouta and Nadeem Al-Salem whose friendship over the last year has been a crucial factor in my survival through graduate school. Our endless nights in the libraries and the long days in Starbucks truly paid off. I wish you all the best in your future endeavors.

A special thanks goes to MIT's varsity tennis team. Practice was the most enjoyable time of the day. Despite the fact that Iba and Manny insisted on making nerdy jokes constantly, I had a lot of fun with you all.

I cannot find the words to express how grateful I am to Marisa Villareal. Living in Boston took a different dimension with you. Most importantly, I owe you gratitude for the optimism, sense of humor and self-confidence you brought out in me. You have simply been a source of inspiration to me.

Last but definitely not least, I dedicate this thesis to my family, which provided me with endless love and trust. To my parents, Elias and Marie Francis, I give a life-size thank you from the heart, and a warm kiss on the forehead, for always believing in me. Your prayers and love have been my source of inspiration and motivation to accomplish the highest goals.

To my brother Dr. Jawad, and my sister Sahar, I extend my love for their support over the years. My regards also go to Dr. John Khalaf for being the perfect brother-in-law, for being an achiever, and a funny and dynamic person. Finally, I would like to acknowledge and embrace my nephew, John Patrick, who has been a source of love and joy for my family.

This work was supported in part by the National Aeronautics and Space Administration (NASA) through the NASA Cooperative Agreement NCC 9-58 with the National Space Biomedical Research Institute and in part by grant R01 EB001659 from the National Institute of Biomedical Imaging and Bioengineering of the United States Institutes of Health.

Contents

1	Introduction	13
1.1	Assessment of Patient State in the Intensive Care Unit	13
1.2	The Cardiovascular System as a Lumped Parameter Model	14
1.2.1	Anatomical characteristics of the systemic arterial circulation	15
1.3	Cardiac Output Monitoring	16
1.3.1	Measurement techniques of cardiac output	16
1.3.2	Model-based cardiac output estimation	17
1.4	Thesis Aims	18
1.5	Thesis Outline	18
2	Windkessel-Type Models	19
2.1	Windkessel Model	19
2.2	Three-Element Windkessel Model	21
2.3	Modified Windkessel Model	22
2.3.1	State space model derivation	23
2.3.2	Previous uses of the Modified Windkessel model	24
2.4	Left Ventricle as a Pulsating Source	25
2.5	Modified Windkessel Model Validation through Forward Modeling	29
2.5.1	Model validation in the time domain	29
2.5.2	Model validation in the frequency domain	30
2.6	Concluding Remarks	35
3	Parameter Space Analysis	37
3.1	Model Parameterization	37
3.2	Sensitivity Analysis	38
3.2.1	Scaling of the parameter sensitivities	39
3.2.2	Deriving the sensitivity matrix	39
3.2.3	An ill-conditioned estimation problem	40

3.3	Subset Selection	41
3.3.1	Subset selection algorithm	42
3.3.2	Subset selection results	42
3.4	The Uncertainty about Arterial Compliance	44
3.4.1	Estimation of a constant compliance	44
3.4.2	Estimation of a pressure-dependent compliance	51
3.5	Approximation of Blood Inertance	53
3.6	Previous Estimation Methods of Resistance	54
3.7	Concluding Remarks	54
4	Beat-by-beat Parameter Estimation	57
4.1	Nonlinear Dependence of Blood Pressure on R_a and Q_{\max}	57
4.1.1	Problem statement	58
4.2	Nonlinear Least Squares Optimization Over One Cardiac Cycle	59
4.2.1	Cost functions	59
4.2.2	Gauss-Newton nonlinear least squares optimization	60
4.2.3	Levenberg-Marquardt algorithm	63
4.2.4	Goodness-of-fit	63
4.3	Continuous Beat-by-Beat Estimation	65
4.3.1	Setting the initial conditions of state space variables	65
4.3.2	Setting C_{ap} , C_{ad} and L	65
4.3.3	Initial guesses of R_a and Q_{\max}	68
4.3.4	Summary diagram	69
4.4	Concluding Remarks	70
5	Results	71
5.1	Description of the Porcine Data	71
5.2	One-Cycle Fitting	72
5.3	Continuous Monitoring of Four Pigs	73
5.4	Statistical Significance of Estimated Parameters	77
5.5	Limitations	78
5.6	Concluding Remarks	79
6	Conclusions and Future Work	81
6.1	Summary	81
6.2	Suggested Improvements to the CO Estimation Algorithm	82
6.3	Plausible Extensions	83

List of Figures

2-1	Two-element Windkessel model.	20
2-2	The three-element Windkessel model.	21
2-3	The modified Windkessel model.	22
2-4	Spencer's original circuit diagram.	24
2-5	Left ventricle as an impulse train.	25
2-6	Left ventricle as a rectangular pulse train.	26
2-7	Left ventricle as a triangular pulse train.	27
2-8	Left ventricle as a parabolic pulse train.	28
2-9	Pig #5 arterial flow and pressure waveforms.	29
2-10	Parabolic fit to porcine blood flow.	30
2-11	Simulated pressure waveforms.	31
2-12	Model's impulse response.	32
2-13	Validation of the transfer function.	32
2-14	Bode plot of two-element Windkessel and the modified Windkessel models.	33
2-15	Fourier decomposition of blood flow and pressure waveforms.	35
3-1	Scaled columns of the sensitivity matrix of pressure to model parameters.	41
3-2	The pulse pressure method algorithm.	45
4-1	NLLS estimation scheme over one heart cycle.	64
4-2	Setting the initial conditions for the state variables of the model.	66
4-3	Grid search over the weak parameters for Pig #5.	67
4-4	Beat-by-beat parameter estimation algorithm.	70
5-1	Typical porcine data recordings.	72
5-2	Beat-by-beat cycle fitting.	73
5-3	Algorithm validation on Pig #5 data.	74
5-4	Algorithm validation on Pig #6 data.	75
5-5	Algorithm validation on Pig #8 data.	75

5-6	Algorithm validation on Pig #9 data.	76
5-7	The estimation error as a function of the MAP.	78
5-8	Linear regression plot for cardiac output estimates for 45,509 beats.	79
5-9	Bland-Altman plot for cardiac output estimates over 45,509 porcine cycles.	80

List of Tables

1.1	Correspondence between circuit components and cardiovascular parameters.	14
2.1	Nominal parameter values of the modified Windkessel model.	25
2.2	Fourier coefficients up to the 4 th harmonic.	35
3.1	Angles between columns of the sensitivity matrix.	41
5.1	Estimation algorithm performance using the RMSNE.	74

Chapter 1

Introduction

1.1 Assessment of Patient State in the Intensive Care Unit

Intensive Care Units (ICUs) have high impact on the survival of critically-ill patients in hospitals. Recent statistics have shown that only 10% of the 5 million patients admitted to ICUs die each year [1]. This is remarkable as ICU patients are usually very unstable due to severe disease e.g multiple organ failure.

The fragile conditions of admitted patients require close monitoring of the affected systems: transducers are used to monitor vital signs continuously, blood samples are analyzed in special laboratories, X-ray images are scrutinized by experts, etc, in order to narrow down the possible causes of the observed symptoms. However, this wealth of information can overload intensivists and lead to otherwise preventable deaths of patients [1].

The cardiovascular system is one of systems which needs to be tracked closely in order to assess the patient's state [2]. It is characterized by several parameters which serve as important indices of cardiac and vascular function. Not surprisingly, extensive research has been conducted to exploit measured cardiovascular variables in order to estimate or otherwise assess variables that are inaccessible to direct measurements. Today's ICUs routinely monitor cardiovascular electrical and mechanical activity. Electrocardiography (ECG) is a common recording of the heart's electrical signals that helps physicians detect abnormal heart rhythms. Blood pressure is commonly monitored at different key locations: arterial blood pressure (ABP) is measured using an arterial line inserted into the radial artery, central venous pressure is measured using a catheter in the superior vena cava to monitor filling pressure at the right atrium, and pulmonary artery pressure is recorded to track left ventricular end-diastolic pressure. There are other crucial variables such as cardiac output (CO), the average amount of blood the heart pumps out per unit time, and arterial tree parameters such as peripheral resistance and arterial compliance which currently cannot be measured continuously

and/or noninvasively. Yet, these indices of cardiovascular performance provide critical information about a patient's state as studies have shown that there is a high correlation between the observed variations in these indices and some pathophysiological conditions [3].

A reliable measurement or estimate of CO could improve decision making in the ICU: under normal conditions, CO is around 5 L/min, while under circulatory shock, it could be less than 2 L/min. Consequently, the level of cardiac output provides critical information to intensivists when assessing a patient's state or diagnosing certain diseases.

1.2 The Cardiovascular System as a Lumped Parameter Model

Many researchers have devised elaborate models to study the dynamics of blood in the arterial circulation [5]. Lumped-parameter models, which are based on simple ordinary differential equations, have been used to scrutinize physiological hypotheses. They model hemodynamic variables of the cardiovascular system such as flow, pressures, and volumes. These models were subjects of numerous identification and parameter estimation studies which permitted researchers to estimate parameters previously impossible to measure directly [44]. Electric circuit analogs of the cardiovascular system may include resistors, capacitors, inductors, diodes, and source generators. Table 1.1 shows how electrical components map to physiological parameters. While some researchers ap-

Electrical Component	Cardiovascular Parameter
Capacitance (F)	Compliance, C (ml/mmHg)
Resistor (Ω)	Resistance, R (mmHg.s/ml)
Current flow (A)	Blood flow, Q (ml/s)
Potential difference (V)	Pressure, P (mmHg)
Inductance (L)	Blood inertance, L (mmHg/(ml.s))
Charge (C)	Volume, V (ml)

Table 1.1: Correspondence between circuit components and cardiovascular parameters.

plied transmission-line theory to model the hemodynamics in the circulatory system, simple models have proved to be more practical in tracking patient's cardiovascular parameters in the ICU [3], [26]. Lumped models, based on the “hand-pumped fire engine theory”, were first introduced by Stephen Hales in 1733, and were popularized by Otto Frank [4] a century later. Frank elucidated the two-element Windkessel model of the arterial tree.

In the following section, we present the physiological relevance of the parameters used to model the arterial circulation from an anatomical point of view.

1.2.1 Anatomical characteristics of the systemic arterial circulation

The arterial circulation is characterized by three basic hemodynamic elements which capture the resistive and elastic properties of the vessels as well as the properties of the fluid: total peripheral resistance, arterial compliance, and blood inertance. In this section, we will introduce the three key parameters and highlight their physiological significance. We will revisit their clinical relevance in Chapter 3.

Arterial resistance: Arterial resistance represents the resistance to blood flow in small vessels, mainly in the arterioles. It captures the relation between pressure drop across a vessel and blood flow through it. Under the assumptions that the flow is steady (laminar flow) and the vessel is rigid and uniform, resistance can be quantified using Poisseuille's law which relates resistance to the geometry (length and radius) of the vessel and the blood viscosity. Specifically,

$$R_a = \frac{8\eta L}{\pi r^4} \quad (1.1)$$

where η is the blood viscosity, L is the length of the rigid vessel, and r is its radius.

Macroscopically, studies have shown that arterial resistance could be determined without knowing the vessel's geometry. Based on Ohm's law, total peripheral resistance reflects the steady component of the arterial load: it is approximated as the ratio of mean pressure to cardiac output. Note that this estimate of resistance is not of a single vessel, but of the entire vascular bed.

Arterial compliance: Arterial compliance is obtained from the pressure-volume relationship of a blood vessel. It is an important determinant of the cardiac load as it measures the change in volume in a vessel for a unit change in transmural pressure:

$$C_a = \frac{\Delta V(P)}{\Delta P} \quad (1.2)$$

Given that the arterial wall has nonlinear elastic properties, compliance is a pressure-dependent quantity [39]: in general, as the pulse pressure increases, compliance decreases leading to a convex V-P relation. Compliance is inversely related to *elastance* which quantifies the stiffness of the arteries. Small arteries are less compliant, and therefore stiffer than large arteries. In fact, almost 65% of total arterial compliance is located in the proximal aorta, the head and upper limb vessels [35]. It has been shown that variations in total arterial compliance are linked to various physiological states, motivating the need for a good compliance assessment. For example, decreased compliance has been observed in aging and hypertension [38], [42].

Blood inertance: Blood inertance, L , represents the effective blood mass which is accelerated and decelerated by the pulsatile pumping of the heart. It captures the relationship between the pressure drop across a vessel and the rate of change of flow as follows:

$$\Delta P = L \frac{dQ(t)}{dt} \quad \text{where} \quad L = \frac{\rho L}{\pi r^2} \quad (1.3)$$

where $Q(t)$ is the blood flow, ΔP is the pressure drop, r is the cross sectional radius of the vessel and ρ is the blood density. Note that L is inversely proportional to r^2 while arterial resistance, R_a , is inversely proportional to r^4 . It can then be concluded that inertance is predominant in large arteries where the resistive effects do not play an important role.

1.3 Cardiac Output Monitoring

The utility of cardiac output as an indicator of patient's state caught the attention of several physicians and clinical researchers who attempted to either directly measure cardiac output or to estimate it from measurements of arterial blood pressure. Currently, the clinical gold standard for the assessment of cardiac output in the ICU is an intermittent, highly invasive measurement via thermodilution.

1.3.1 Measurement techniques of cardiac output

Investigators have developed various schemes to measure cardiac output: thermodilution, Doppler ultrasound, and a flowmeter, amongst others.

1. **Thermodilution:** Cold saline is injected at the pulmonary artery to create a thermal deficit and the rate of change in temperature downstream at a distal artery is measured. Cardiac output is inversely related to the area under the resultant temperature-time curve. It is a highly invasive procedure, possibly increasing a patient's instability, as a Swan-Ganz catheter must be advanced through the vena cava and the right heart to the pulmonary artery. In today's ICUs, thermodilution is performed on critically-ill patients and requires experienced operators.
2. **Doppler ultrasound:** This method takes advantage of the relation between stroke volume and the velocity of blood across the aorta, $v(t)$, which can be measured via Doppler ultrasound. Specifically,

$$CO = HR \times SV \quad \text{where} \quad SV = A \int_T v(t) dt \quad (1.4)$$

where A is the cross sectional area of the aorta. Although it requires expensive equipment in addition to a trained ultrasound technician, it is the only scheme which measures cardiac

output non-invasively.

3. **Flowmeter:** An ultrasonic flow probe is placed around the aorta to report instantaneous flow levels. Stroke volume, and consequently cardiac output, can be obtained by integrating the resulting flow waveforms. Contrary to its apparent simplicity, it is a highly invasive procedure as the placement of flowmeter requires thoracotomy. It is only used for research purposes in animal studies.

Although the above methods can be very reliable and accurate, the benefit of measuring cardiac output comes at high cost: for some procedures the incurred cost is from their invasiveness which exposes critically-ill patients to higher risk, while for other procedures the cost is due to the expense of the methods themselves. Consequently, researchers have proposed a different approach to assess cardiac output, namely to derive estimates of CO from arterial blood pressure waveforms which are routinely measured.

1.3.2 Model-based cardiac output estimation

The possibility of estimating cardiac output from measurements of ABP has been extensively researched. At a first glance, the estimation problem is easily solved. However, it rapidly becomes clear that the complexity of the estimation problem is dominated by the complex relationship between CO and ABP. Till now, there is no consensus on a single relationship between pressure and cardiac output or even on the performance of the algorithms that have been proposed in the past. Sun *et al.* [13], for example, developed an algorithm that applies 11 reasonably accepted methods of estimating CO from peripheral ABP recordings to 120 patients from the MIMIC II database [24]. He concluded that Liljestrand and Zander's method [7] for computing a pressure-dependent compliance for the two-element Windkessel model yields the most accurate CO estimates from ABP waveforms.

More recent approaches, not covered in Sun's work, have been developed to continuously estimate CO along with other cardiovascular variables from the beat-to-beat fluctuations in ABP waveforms. Blind source identification is an approach adopted by Reisner *et al.* [10] and Mukkamala *et al.* [11] to obtain continuous CO estimates from multiple peripheral pressure waveforms. Mukkamala and co-workers suggested an alternative scheme which uses inter-beat fluctuations in ABP waveforms to quantify relative variations in cardiac output [12]. Cycle-averaged techniques are currently being explored by Parlikar *et al.* [18], [19] to obtain beat-to-beat estimates of cardiac output from peripheral ABP waveforms.

1.4 Thesis Aims

This thesis is aimed at characterizing heart function (in terms of CO and TPR) using ABP waveforms in the modified Windkessel model. The thesis objectives are as follows:

1. To provide an exhaustive literature review of Windkessel-type models and related parameter estimation algorithms.
2. To develop an estimation method for computing beat-to-beat estimates of CO and TPR by capturing intra-beat dynamics of ABP waveforms.
3. To validate the performance of CO estimation method on porcine data.

1.5 Thesis Outline

The thesis is organized as follows:

1. Chapter 2, *Windkessel-Type Models*, presents the theory of the two-element Windkessel model and discusses more complex variations, the three-element Windkessel model and the modified Windkessel model. It highlights possible choices for simulating the left ventricle and validates the modified Windkessel model.
2. Chapter 3, *Parameter Space Analysis*, develops a sensitivity analysis platform followed by a detailed literature review of methods for parameter estimation in Windkessel-type models.
3. Chapter 4, *Beat-by-Beat Parameter Estimation*, explains the theory behind nonlinear least squares optimization and presents our method for estimating CO and TPR. It then summarizes the details of a continuous estimation scheme.
4. Chapter 5, *Results*, presents the performance of our CO estimation algorithm on porcine data.
5. Chapter 6, *Conclusion and Future Work*, discusses the limitations and advantages of our estimation algorithm and suggests possible improvements for future work.

Chapter 2

Windkessel-Type Models

The cardiovascular system has been extensively studied over the centuries. In 1899, Otto Frank formulated the concept of cardiac work through one of the earliest modeling approaches in cardiovascular physiology. Subsequently, his theory of the Windkessel model was employed by many researchers to develop electrical and mechanical analogs in order to understand and predict the behavior of the cardiovascular system. In a study by Campbell *et al.* [28], it was observed that as the number of parameters increases in a Windkessel model, the parameter predictions and the waveform fits to experimental data were improved. However, the challenge remains to identify all parameters in complex models so to obtain good pressure and flow waveform fits. In this chapter, we will first present the original Windkessel model, followed by the three-element variation of the Windkessel model before introducing and analyzing the model of interest, the modified Windkessel model. We then explore the effect of four different pulse shapes for blood flow into the arterial tree on the shape of the arterial pressure waveforms. Finally, we validate the choice of pulse shape and the modified Windkessel model through forward modeling.

2.1 Windkessel Model

The Windkessel model developed by Otto Frank represents the heart as a current source that pumps blood into the arterial system, which is lumped into a single resistance and a single compliance [4]. The electric circuit analog of the Windkessel model, shown in Figure 2-1, simulates blood pressure dynamics in the systemic arteries. This two-element Windkessel was introduced with an impulse train as the input to simulate the pumping heart. The area of each impulse represents the stroke volume, which is the amount of blood ejected by the left ventricle during each cardiac cycle.

The heart pumps blood into the vessels during systole through the aorta. The ejected blood circulates through the arteries, represented by a capacitance corresponding to the elastic properties of all the arteries combined, and a resistance to flow, resulting from viscous dissipation in the

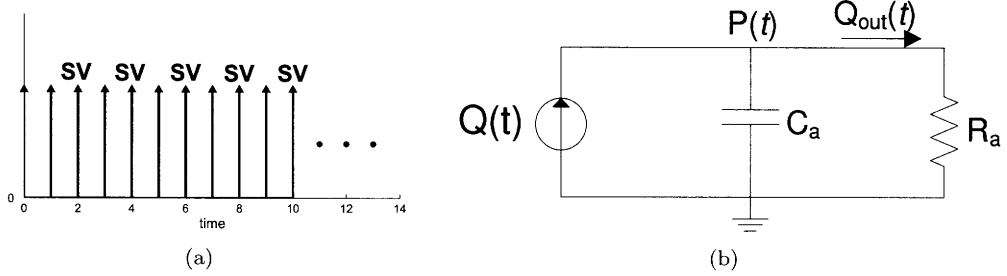


Figure 2-1: a) Left ventricle outflow modeled as an impulse train. b) The Windkessel model of the arterial system.

arterioles captured in the Windkessel model by the dissipation of the energy stored in the capacitor through the resistance. This model simulates the aortic pressure waveform as an exponential decay during diastole which approximates real pressure waveforms in large arteries. The time constant of the decay is determined by the product of resistance and the compliance.

Mathematical framework: The flow continuity equation applied to the Windkessel model yields

$$\frac{dV(t)}{dt} = Q(t) - Q_{out}(t) \quad (2.1)$$

where V is the arterial blood volume. $Q(t)$ corresponds to the current source in the two-element Windkessel model. $Q_{out}(t)$ is the flow through the arterioles (the resistor). Since outflow of blood is observed at the resistance R_a ,

$$Q_{out}(t) = \frac{P(t)}{R_a} \quad (2.2)$$

where $P(t)$ is the pressure drop across the resistance. In the case of a linear pressure-volume relationship for the arterial system, total arterial compliance can be written as

$$C_a = \frac{dV(t)}{dP(t)} \quad (2.3)$$

Substituting Eq. 2.2 and Eq. 2.3 in Eq. 2.1 results in the governing Eq. 2.4 for the two-element Windkessel.

$$Q(t) = C_a \frac{dP(t)}{dt} + \frac{P(t)}{R_a} \quad (2.4)$$

Eq. 2.4 can be interpreted as follows: the heart forces blood out of the ventricle, some of which charges the capacitor, or in other words inflates the large proximal arteries, and the rest dissipates through the resistance.

Although this model has been used by many researchers as a good approximation of the arterial system's behavior, it has some obvious limitations when used to model peripheral arterial blood

pressures. One of its major weaknesses is that it does not account for the propagation effects through the vessels: it assumes that the pressure rise occurs simultaneously in the entire arterial tree [27]. However, the properties of the distal vessels influence the shape of the peripheral arterial pressure waveform. The model also implies infinitely high wave speed in diastole and ignores the effect of wave reflections on pressure waveforms. Another obvious limitation of the two-element Windkessel model, which will be revisited in Section 2.5.2.2, is that it accurately captures only the behavior of the input impedance as seen by the left ventricle at low frequencies but fails at higher frequencies [34]. Consequently, a more detailed model is needed to account for the wave propagation effects and the high frequency behavior of the arterial input impedance when building a model for radial pressure waveform characterization.

2.2 Three-Element Windkessel Model

A three-element Windkessel model was proposed by Westerhof [29] to mimic the arterial load faced by the pumping left ventricle of the heart. Based on the observations of the human cardiovascular system, the arterial tree is characterized by an input impedance which has some well-known features. The magnitude of the input impedance, Z_{in} , is large at DC and decreases rapidly for frequencies as low as 3 Hz [29]. It then remains fairly constant for higher frequencies. The phase however, is observed to be zero at DC, negative for low frequencies and approximately zero for high frequencies [29]. The original Windkessel model does not translate these properties reliably at all frequencies: at high frequencies, the input impedance as modeled by the two-element Windkessel provides a poor representation of the actual aortic impedance [34]. Figure 2-2 shows the three-element model as proposed by Westerhof.

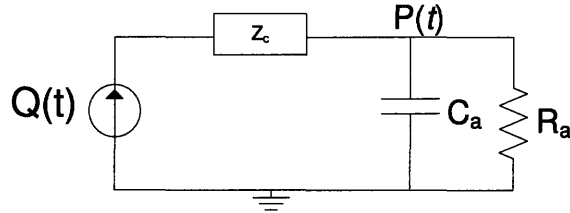


Figure 2-2: The three-element Windkessel model developed by Westerhof.

It consists of a characteristic impedance, Z_c , in series with a parallel arrangement of total arterial compliance, C_a , and systemic vascular resistance, R_a . The input impedance then becomes:

$$Z_{in} = Z_c + \frac{R_a}{1 + jwR_aC_a} \quad (2.5)$$

Z_c was introduced to account for the effects of inertia and proximal arterial compliance at high

frequencies. For large arteries, Z_c can be represented as $\sqrt{\frac{L}{C_{ap}}}$ where L is blood inertance per unit length and C_{ap} is the proximal compliance per unit length.

The governing equation given the circuit topology in Figure 2-2 and an assumed flow waveform $Q(t)$ is

$$P(t) + R_a C_a \cdot \frac{dP(t)}{dt} = (R_a + Z_c) \cdot Q(t) + Z_c R_a C_a \cdot \frac{dQ(t)}{dt} \quad (2.6)$$

where $P(t)$ is the pressure across the resistor. This model has undergone extensive research: Wesselung [51] investigated the applicability of the three-element Windkessel model for the reconstruction of the cardiac flow waveform from peripheral blood pressure waveforms. Noordergraaf *et al.* [52] attempted to estimate the effective length of the arterial system using this variation of the Windkessel model.

So far, we have presented the original two-element Windkessel model and a higher order three-element model whose complexity is defined by that of the characteristic impedance. Subsequent researchers aimed to replace Z_c it by different configurations of resistances, compliances and inertance components. One successful attempt lead to the development of the modified Windkessel model which is described in detail in the following section.

2.3 Modified Windkessel Model

The modified Windkessel model (MWK) is one of the most widely used variations of the three-element Windkessel. It is one of the simplest models which faithfully reproduce intra-beat variations in pressure waveforms. It lumps the arterial tree into two major compartments, proximal and distal. Figure 2-3 shows the electric analog of the modified Windkessel model intended to approximate the

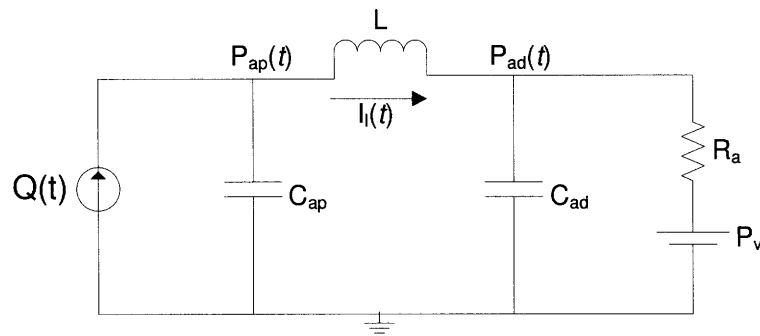


Figure 2-3: The modified Windkessel circuit model. C_{ap} represents the elastic capacitance of large arteries close to the heart, while C_{ad} represents that of muscular arteries further away from the heart. L represents the inertance of the flowing blood. R_a represents the peripheral resistance and P_v represents a constant venous pressure component.

radial pressure waveform. Given that properties of the distal arteries differ from those close to the heart, it is advantageous to split the whole-body compliance used in the original Windkessel into

two: the compliance of large elastic arteries, C_{ap} , and the compliance of the more muscular distal arteries, C_{ad} . In fact, the small arteries which are further away from the heart are stiffer than the elastic arteries and consequently, their capacitance is much smaller than that of large arteries. The latter was shown by Watt and Burrus [47]. A study by Rietzchel *et al.* [48] confirmed that C_{ad} corresponds to the compliance of distal arteries due to its sensitivity to vasodilatory experiments, a property not apparent for C_{ap} . Clinical studies have shown that C_{ad} is reduced with aging, hypertension or diabetes which makes it a good indicator of cardiovascular risk [50].

The modified Windkessel model accounts for the flow propagation effects by introducing an inductor L between the two capacitances representing blood inertance along the fluid column. Neglecting resistive losses, the pressure difference between the two extremes of a vessel is proportional to the acceleration of the blood as it moves from one end to another by a factor equal to the blood inertance. Also, the model lumps the venous circulation into a constant pressure source, P_v , which is equal to the downstream pressure, assumed to be mean venous pressure. The pumping heart is modeled as a pulsating current source as will be discussed in detail in Section 2.4.

2.3.1 State space model derivation

Given that the model is composed of three energy storage elements, a state space model with three states is sufficient to fully describe the dynamics of the system. Using Kirchhoff's voltage and current laws, KVL and KCL respectively, we obtain the following three equations:

$$Q(t) = C_{ap} \cdot \frac{dP_{ap}(t)}{dt} + I_l(t) \quad (2.7)$$

$$\frac{dI_l(t)}{dt} = \frac{P_{ap}(t)}{L} - \frac{P_{ad}(t)}{L} \quad (2.8)$$

$$I_l(t) = C_{ad} \cdot \frac{dP_{ad}(t)}{dt} + \frac{P_{ad}(t) - P_v}{R_a} \quad (2.9)$$

where $P_{ap}(t)$ is the voltage across C_{ap} , $P_{ad}(t)$ the voltage across C_{ad} , and $I_l(t)$ the current through the inductor, L . The input to the system is $Q(t)$. The resulting state space model is then:

$$\frac{d}{dt} \begin{bmatrix} P_{ap}(t) \\ I_l(t) \\ P_{ad}(t) \end{bmatrix} = \begin{bmatrix} 0 & -\frac{1}{C_{ap}} & 0 \\ \frac{1}{L} & 0 & -\frac{1}{L} \\ 0 & \frac{1}{C_{ad}} & \frac{-1}{R_a C_{ad}} \end{bmatrix} \begin{bmatrix} P_{ap}(t) \\ I_l(t) \\ P_{ad}(t) \end{bmatrix} + \begin{bmatrix} \frac{Q(t)}{C_{ap}} \\ 0 \\ \frac{P_v}{R_a C_{ad}} \end{bmatrix} \quad (2.10)$$

which can easily be implemented on a digital computer.

By rearranging the third state equation and substituting the resulting expression for $I_l(t)$ in the

first state equation, we get the input/output equation of the model:

$$C_{ap} \cdot \frac{dP_{ap}(t)}{dt} + C_{ad} \cdot \frac{dP_{ad}(t)}{dt} + \frac{P_{ad}(t)}{R_a} = Q(t) \quad (2.11)$$

If we were to assume that the voltage drop across the inductor is negligible ($P_{ad}(t) \approx P_{ap}(t)$), then Eq. 2.11 reduces to the governing equation of the two-element Windkessel model, Eq. 2.4 with $C_a = C_{ad} + C_{ap}$.

2.3.2 Previous uses of the Modified Windkessel model

Resonant circuits have been widely used in the literature to capture the dynamics of the radial pressure waveform. For instance, Burattini *et al.* [43] analyzed models with different frequency responses to determine the order of the necessary lumped model to faithfully represent the behavior of the arterial system. Spencer *et al.* [6] developed in 1963 the first version of the modified Windkessel model, shown in Figure 2-4, in order to generate aortic and femoral pressure waveforms simultaneously.

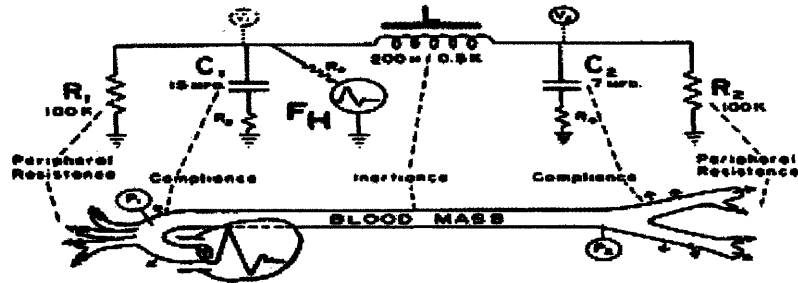


Figure 2-4: First version of the modified Windkessel model adapted from the *Handbook of Physiology* by Spencer [6].

In 1967, Goldwyn and Watt [27] formally introduced the modified Windkessel model and the diastolic decay method, which will be discussed in detail in Section 3.4.1.3. In 1976, Watt and Burrus proposed a Gauss-Newton least-squares estimation method for the identification of model parameters [47]. Clark *et al.* [8] developed an estimation scheme of the parameters of the modified Windkessel based on three distinct arterial pressure measurements and an estimate of cardiac output. Guarini *et al.* [9] used this model to determine the best left-ventricular model function and its optimum parameter values using radial pressure waveforms and cardiac output. Segers *et al.* [50] applied their proprietary pulse pressure method for the estimation of arterial compliance in the modified Windkessel model.

While this third-order model has been extensively used to estimate parameters characterizing the arterial tree, most methods required the measurement of flow and pressure as will be discussed

in Section 3.4. Since flow measurements are invasive, the applicability of these methods is limited in clinical settings. The latter observation justifies the need for a method which estimates cardiac output and resistance with minimal invasiveness from pressure measurements.

2.4 Left Ventricle as a Pulsating Source

So far, we have considered the left ventricle to eject blood in an impulsive manner. However, the assumed shape of the pulsatile flow is critical to the left ventricle's flow dynamics. In this section, we explore four different blood flow waveforms which will be evaluated through qualitative validation of the resulting pressure waveforms. We will fix the modified Windkessel model's parameters at some nominal values that are representative of healthy humans, summarized in Table 2.1.

Parameter	Nominal value
C_{ad}	0.15 ml/mmHg
C_{ap}	1.45 ml/mmHg
R_a	1.0 mmHg.s/ml
L	0.025 mmHg/(ml.s)
SV	80 ml/beat
HR	60 bpm

Table 2.1: Nominal parameter values of the modified Windkessel model.

Left ventricle outflow as a impulse train: The Windkessel model was derived using an impulse current source in which the area of each impulse is equal to the stroke volume of the heart (under normal conditions about 80 ml/beat).

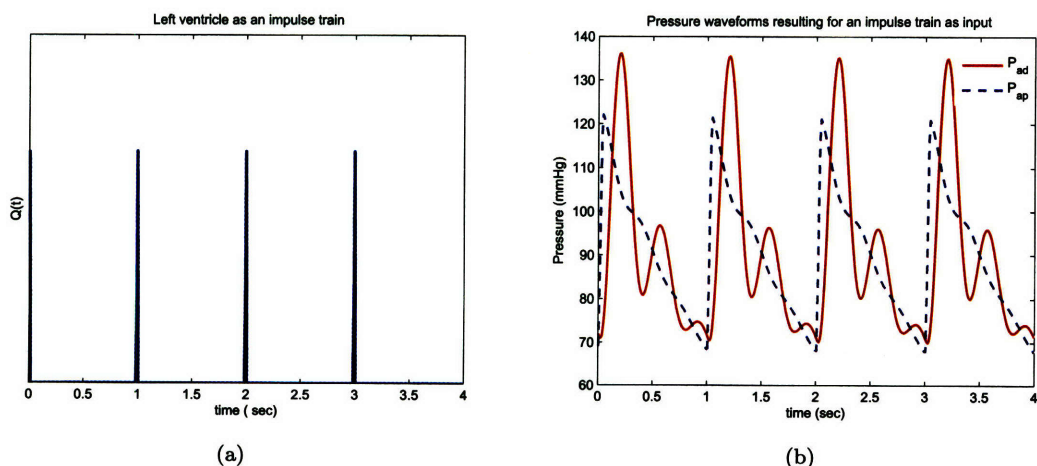


Figure 2-5: a) Left ventricle as a impulse train source, where each impulse is of magnitude of 80 ml/beat; b) proximal (dashed) and distal (solid) artery pressure responses to an impulse input in the modified Windkessel model.

Specifically,

$$Q(t) = \sum_k SV_k \cdot \delta(t - t_k) \quad (2.12)$$

where SV_k is the stroke volume of the k^{th} cycle, and t_k s the onset time of the k^{th} cycle.

When tested with the modified Windkessel, the resulting pressure waveforms did not resemble the shape of physiologic waveforms. Figure 2-5 shows that the impulsive current source gives a poor representation of the pumping heart: the large magnitude of the generated pulse pressure, the sharper notch in the peripheral pressure waveform, and the sharper peak in the aortic pressure waveform are all evidence that a better characterization of the pumping heart is required. The state space model illustrates the dependency of the rate of change of proximal pressure, $\frac{dP_{ap}(t)}{dt}$, on the instantaneous flow, $Q(t)$: at the onset of each beat, $Q(t)$ is very large which translates into an almost infinite slope in the proximal pressure waveform.

Since the stroke volume is ejected throughout systole, wider pulse trains over systole were considered to capture the ejection behavior of the left ventricle better.

Left ventricle outflow as a rectangular pulse train: A pulse-shaped source was then tested such that flow is given by:

$$Q(t) = \sum_k \frac{SV_k}{T_s} \left(u(t - t_k) - u(t - (t_k + T_s)) \right) \quad (2.13)$$

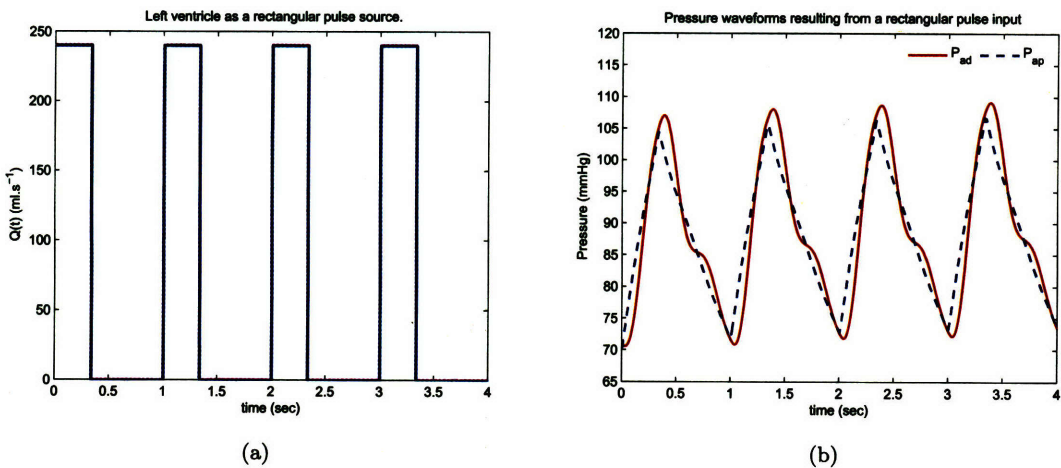


Figure 2-6: a) Left ventricle as a rectangular pulse of height 240 ml/s and width $\frac{1}{3}\sqrt{T}$ sec; b) proximal (dashed) and distal (solid) artery pressure responses.

The resulting output can be seen in Figure 2-6. The pulsating source results in pressure waveforms which illustrate many of the characteristics exhibited by physiologic data such as the smooth notch in the distal pressure waveform. However, the peak-to-peak magnitude of each waveform is less than the peak-to-peak amplitude observed in measured data. Moreover, the maximum pressure peaks

occur at the end of systole while recorded waveforms show that pressure peaks occur before the end of systole.

Consequently, other pulse shapes are tradeoffs between impulsive flow and constant flow during systole. A right angle triangle was considered to capture the large peak-to-peak value of the pressure waveforms from impulsive flow and the smooth notch from rectangular pulse flow.

Left ventricle outflow as a triangular pulse train: A more suitable source might be a right angle triangle (Figure 2-7) whose height is adjusted so that its area equals stroke volume. Specifically,

$$Q(t) = \sum_k \left(\frac{-2.SV_k}{T_s^2} (t - t_k) + \frac{2.SV_k}{T_s} \right) \left(u(t - t_k) - u(t - (t_k + T_s)) \right) \quad (2.14)$$

Such pulsatile flow is easily parameterized since the height of the triangle, Q_{\max} , and the width of the base, T_s , are sufficient parameters to characterize the entire flow waveform. Studies of arterial flow have concluded that the duration of systole, T_s , is best approximated in humans by $\frac{\sqrt{T}}{3}$ [21]. Hence, T_s is calculated from heart rate and the only remaining unknown is Q_{\max} .

Triangular sources have been previously explored by Segers *et al.* [30], [35] and validated as an alternative to measured flow by comparison of their frequency contents. However, in their studies, maximum flow, Q_{\max} , was assumed at $t = \frac{T_s}{3}$ instead of at the onset of the beat.

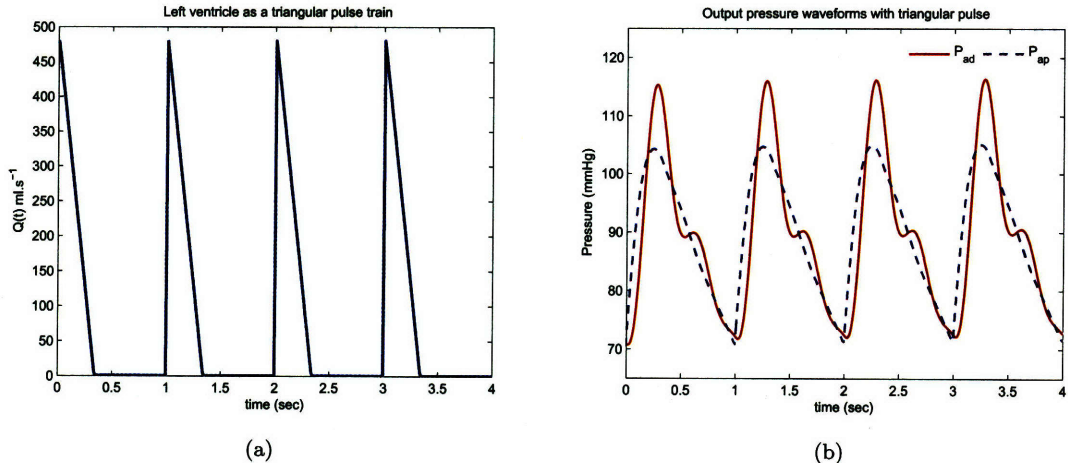


Figure 2-7: a) Left ventricle as a triangular pulse source, b) distal artery pressure (solid), and proximal artery pressure responses (dashed).

Figure 2-7 shows the response of the modified Windkessel model to a right angle triangular pulse train input.

Left ventricle outflow as a parabolic pulse train: Although the triangular flow discussed above resulted in well-behaved pressure waveforms, there is no physiologic explanation why such a shape should be assumed for flow. Instead, by inspecting flow waveforms from porcine recordings,

it became apparent that a parabolic flow would be more suitable to fit measured arterial flow waveforms. The parabola can be described by two parameters similarly to the triangular pulse. Assuming flow is exactly zero during diastole, the general form of parabolic flow is:

$$Q(t) = \sum_k \left(a(t - t_k)^2 + b(t - t_k) \right) \left(u(t - t_k) - u(t - (t_k + T_s)) \right) \quad (2.15)$$

where

$$a = \frac{-6 \cdot SV_k}{T_s^3} \quad b = \frac{6 \cdot SV_k}{T_s^2} \quad (2.16)$$

The maximum flow, Q_{\max} , occurs at $\frac{T_s}{2}$ and the corresponding value is

$$Q_{\max} = \frac{3T_k}{2T_s} \cdot CO_k = \frac{-a \cdot T_s^2}{4} \quad (2.17)$$

Figure 2-8 shows flow as a parabolic pulse and the resulting pressure waveforms. It can be concluded from observing the morphology of the pressure waveforms that parabolic flow leads to well-behaved pressure waveforms while still preserving the physiologic properties of the flow waveform.

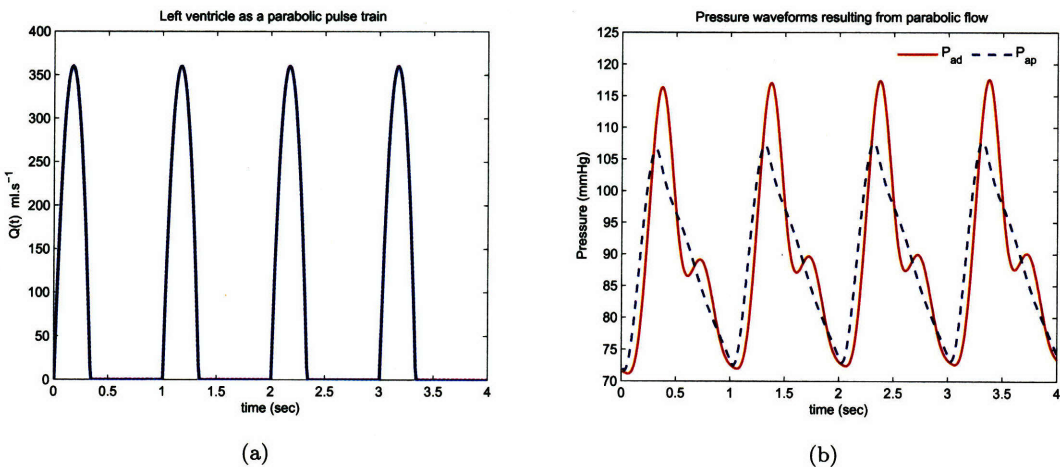


Figure 2-8: a) Left ventricle as a parabolic pulse source; b) pressure waveforms in response to parabolic flow: distal artery pressure (solid), and proximal artery pressure (dashed).

In the next section, we validate the modified Windkessel model by comparing the simulated pressure waveforms to measured waveforms.

2.5 Modified Windkessel Model Validation through Forward Modeling

The modified Windkessel model presented above is the basis of the mathematical framework which we use to estimate cardiac output and arterial resistance as will be discussed in Chapter 4. In this section, we validate the input pulse shape and the output pressure waveforms through forward modeling. While we had access to human data provided by the MIMIC II database [24], time and frequency domains validation was conducted on porcine data collected at MIT [12]. Figure 2-9 shows a portion of continuous pressure and arterial flow waveforms from pig #5.

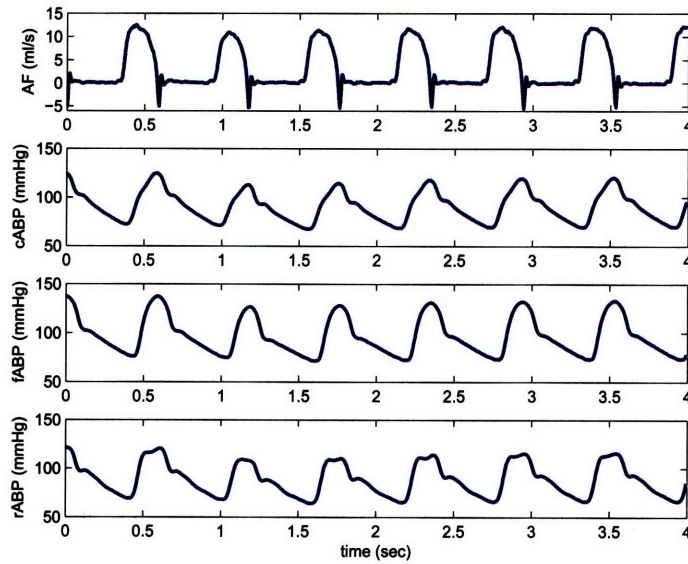


Figure 2-9: Pig #5 arterial flow and pressure waveforms.

2.5.1 Model validation in the time domain

Validation of parabolic flow: In Section 2.4, different pulse shapes were presented and their ability to characterize arterial flow was discussed. We concluded that parabolic flow provided the best flow morphology. In Figure 2-10, we show one cycle of measured arterial flow, AF, and the simulated parabolic flow. Measured AF exhibits reflective flow at the aorta due to the closure of the aortic valve. We ignore the negligible diastolic retrograde flow. The resulting fit may then underestimate or overestimate the stroke volume for the corresponding beat, which makes it impossible to perfectly account for the entire flow dynamics.

In Section 2.4, we qualitatively validated the pressure waveform as the response of the modified Windkessel model to parabolic flow. In the following paragraph, we compare measured pressure

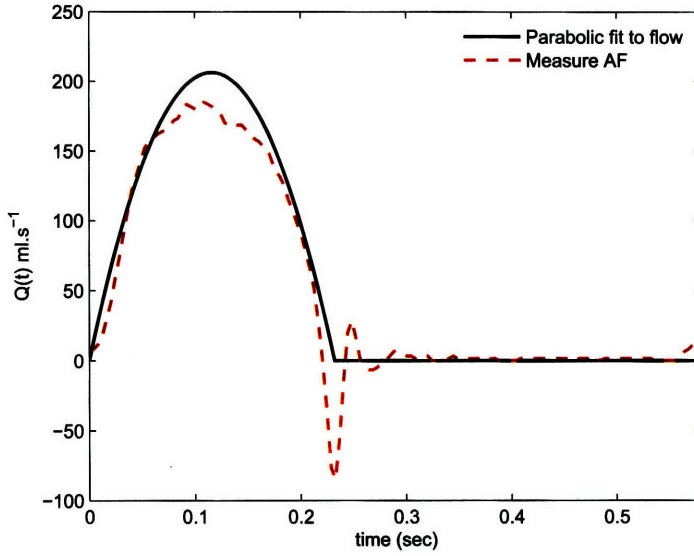


Figure 2-10: Measured arterial flow (dashed) and the corresponding fit using parabolic shape (solid).

waveforms to the model's pressure outputs.

Pressure waveform fits: While the use of the modified Windkessel model was motivated by its ability to capture oscillatory behaviors in diastole, it was observed that it best represents porcine distal pressure waveforms when measured at the femoral artery where pressure waves do not exhibit as many reflections as at the radial artery. Measured radial artery pressure waveforms, $r\text{ABP}$, are difficult to capture due to the high reflective nature of the measured waveforms. Most $r\text{ABP}$ waveforms qualify as Type A beats where the first peak is lower than the following one [31]. Figure 2-11 shows the resulting fits to a central aortic pressure beat and a femoral arterial pressure beat. It can be seen that, for a well chosen set of parameter values, the modified Windkessel model yields good fits to both proximally and distally measured pressure waveforms. The systolic portion of the measured pressure cycle in Figure 2-11 are well captured at both locations. The only major discrepancy is observed in the diastolic representation of the distal pressure: the notch in the modeled distal pressure is not as damped as in the measured femoral artery pressure, $f\text{ABP}$.

2.5.2 Model validation in the frequency domain

Many studies have focused on frequency domain methods to determine transfer functions that characterize the transformation between pressure waveforms from different sites in the arterial system [14], [15]. In analyzing the modified Windkessel model, we treat it as a linear time invariant (LTI) system. Since exponentials are eigenvectors of LTI systems, the Fourier decomposition of the output can be calculated by multiplying the Fourier coefficients of the input by the transform of the impulse

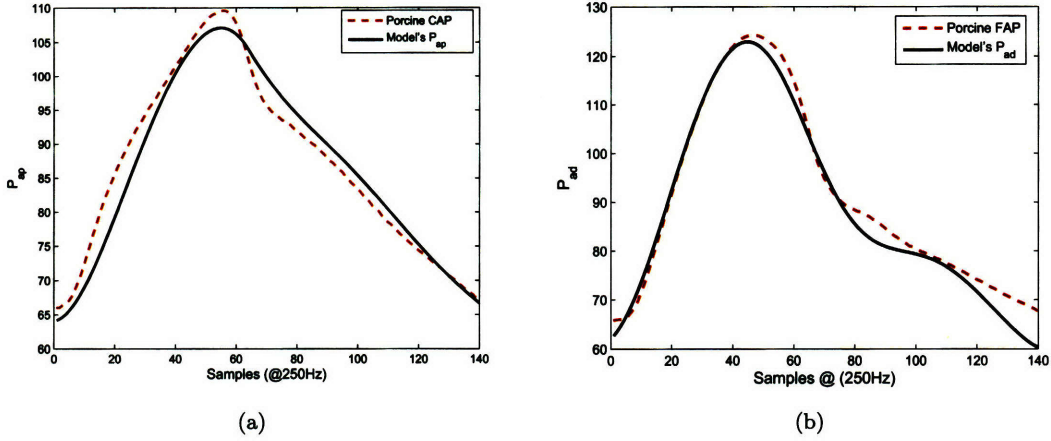


Figure 2-11: a) Central aortic pressure and b) femoral arterial pressure generated by the modified Windkessel model.

response of the system. Following the work of many researchers who analyzed Windkessel-type models in the frequency domain, we validate the modified Windkessel model's setup as presented above by deriving the system's transfer function and analyzing its response to a parabolic input function.

2.5.2.1 Derivation of the system's transfer function

Given that the system has two sources, the current source representing the heart and the constant venous pressure P_v , the transfer function of the system with input $Q(s)$ and output $P_{ad}(s)$ can be determined by superposition as follows:

$$P_{ad}(s) = H_1(s)P_v(s) + H_2(s)Q(s) \quad (2.18)$$

where $H_1(s)$ and $H_2(s)$ are the transfer functions relating the distal pressure to $P_v(s)$ and $Q(s)$ respectively. The resulting expression for P_{ad} becomes

$$P_{ad}(s) = \frac{P_v \frac{LC_{ap}s^2 + 1}{s} + R_a Q(s)}{1 + R_a(C_{ap} + C_{ad})s + LC_{ap}s^2 + LC_{ap}C_{ad}R_a s^3} \quad (2.19)$$

$$\text{where } P_v(s) = \frac{P_v}{s} \quad (2.20)$$

When setting P_v to 0 mmHg, $P_{ad}(s)$ can be obtained by simply substituting the transform of the input, $Q(s)$, into the transfer function above. The impulse response of the system, when P_v is 0 mmHg, is shown in Figure 2-12. Note that it corresponds to the impulse response of the modified Windkessel model with the parameters set at values corresponding to pig #5 from our data set during the initial steady state, ($R_a = 1.814$, $C_{ad} = 0.045$, $C_{ap} = 0.35$ and $L = 0.04$).

The impulse response is characterized by a damped ringing with a period of $T \simeq 0.27$ sec.

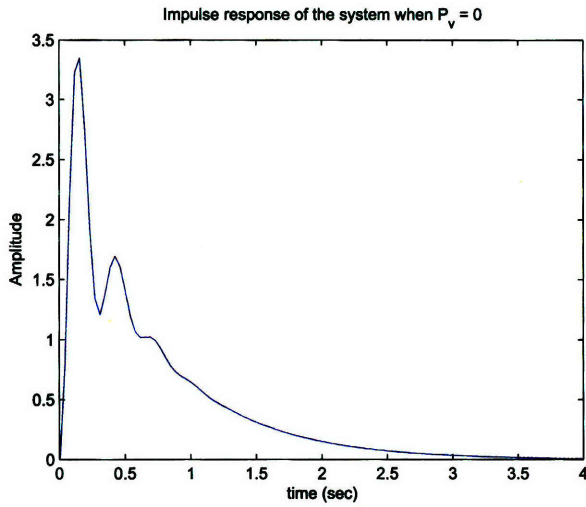


Figure 2-12: The impulse response of the system when $P_v = 0$ mmHg.

This ringing is due to the exchange of energy between the inductor L and the distal compliance C_{ad} . The natural frequency of the system is equal to $\frac{1}{\sqrt{(LC_{ad})}}$, which is equivalent to a period of $2\pi\sqrt{(LC_{ad})} \simeq 0.27$ sec. The exponential decay has a time constant that is almost equal to $R_a(C_{ap} + C_{ad}) = 0.72$ sec.

As a validation scheme of the transfer function, the system's impulse response was convolved with the parabolic pulse train, shown in Figure 2-8 and then added to the impulse response of the contribution of P_v . Figure 2-13 shows the resulting output. The output is mathematically described by

$$P_{ad}(t) = L^{-1}\{H_1(s)P_v(s)\} + h_2(t) * Q(t) \quad (2.21)$$

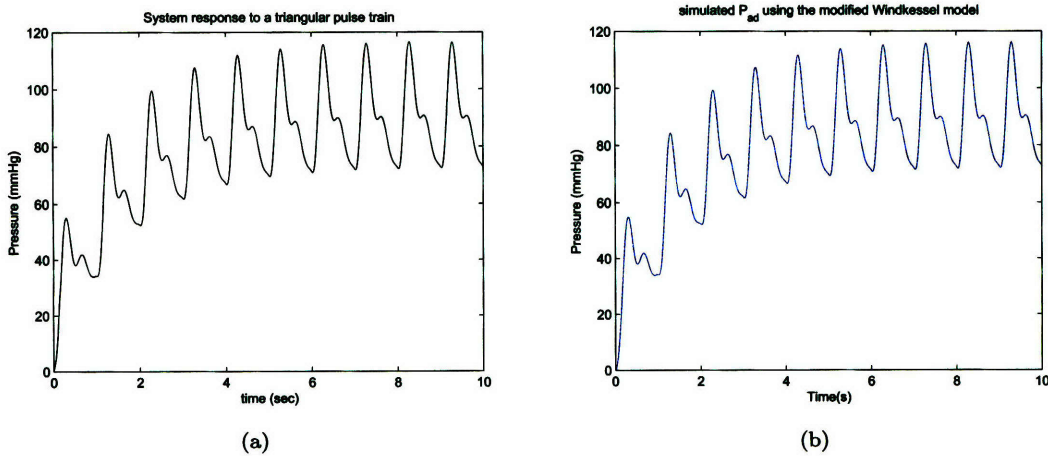


Figure 2-13: a) $P_{ad}(t)$ resulting from convolving the impulse response of the system with a parabolic input. b) $P_{ad}(t)$ resulting from solving the simulation with parabolic flow.

where $h_2(t)$ is the impulse response of the modified Windkessel model relating blood flow to distal pressure. Comparing the pressure waveforms in Figure 2-13, it can be seen that the waveform resulting from the convolution with the impulse response contains the basic information of the state-space model output $P_{ad}(t)$.

2.5.2.2 Comparison with two-element Windkessel

While there are many limitations of the two-element Windkessel, it has been argued that models with higher complexity do not necessarily have great impact on the goodness of the resulting pressure waveform fits. This is mainly due to the narrow range of the frequency content of analyzed signals. The transfer function of the modified Windkessel model, when P_v is set to zero, is

$$\frac{P_{ad}(s)}{Q(s)} = \frac{\frac{1}{LC_{ap}C_{ad}}}{\frac{1}{LC_{ap}C_{ad}R_a} + \frac{C_{ap}+C_{ad}}{LC_{ap}C_{ad}}s + \frac{1}{R_aC_{ad}}s^2 + s^3} \quad (2.22)$$

At low frequencies, Eq. 2.22 can be approximated as

$$\frac{P_{ad}(s)}{Q(s)} \approx \frac{\frac{1}{C_{ap}+C_{ad}}}{s + \frac{1}{R_a(C_{ap}+C_{ad})}} \quad (2.23)$$

Since the frequency content of pressure waveforms is most dense over the first three harmonics,

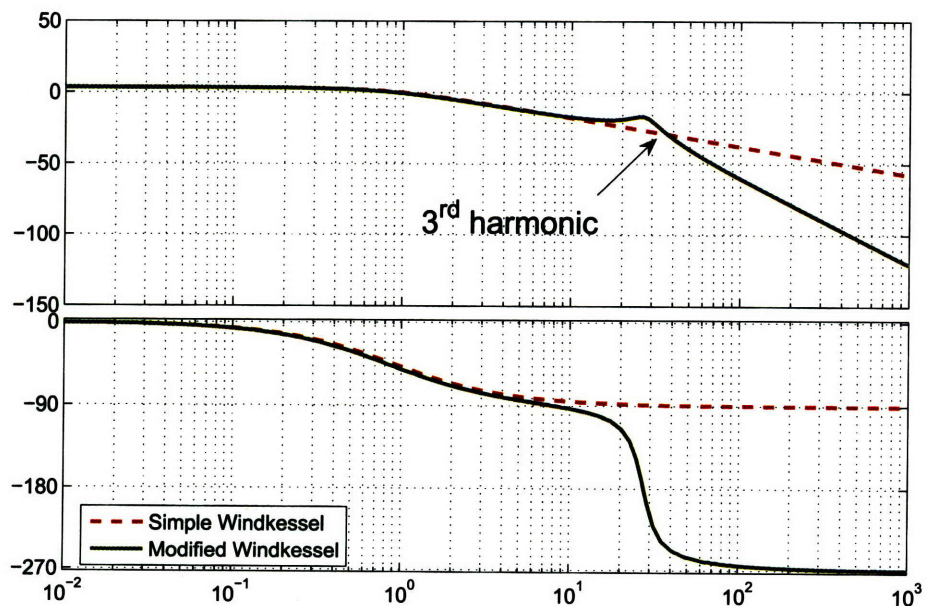


Figure 2-14: Comparison of the Bode plots of the transfer function of the Windkessel Model and that of the modified Windkessel model.

the use of the two-element Windkessel as a reasonable model of the arterial tree is justified. At low frequencies, the simple Windkessel model and the modified Windkessel model have the same transfer function. Figure 2-14 shows the magnitude and phase of the transfer functions for both models. The models diverge for frequencies greater than 12 Hz. However, it is hoped that this discrepancy, and specifically the differences in the phase plots, will improve the fit of distal pressure waveforms which exhibit wave reflections and propagation effects.

From the heart's perspective, the input impedance faced by the outflow of the left ventricle is given for the modified Windkessel model as follows:

$$Z_{\text{in}} = \frac{R_a C_{\text{ad}} s^2 + L s + R_a}{R_a L C_{\text{ad}} C_{\text{ap}} s^3 + L C_{\text{ap}} s^2 + R_a (C_{\text{ad}} + C_{\text{ap}}) s + 1} \quad (2.24)$$

The input impedance in Eq. 2.24, calculated at some nominal values of the parameters, has two zeros and three poles. However, it was shown by Watt and Burrus [47] that the two zeros lie on top of two poles, leading to a first order system, the one described by the two-element Windkessel with input impedance.

$$Z_{\text{in}} = \frac{R_a}{1 + R_a C_a s} \quad (2.25)$$

This is mainly due to the effect of the much higher storage ability of proximal arteries which masks the effect of distal compliance as well as the blood inertance.

2.5.2.3 Fourier analysis

As mentioned above, exponentials are eigenfunctions of this system's transfer function. We tested whether processing the k^{th} harmonic of the input yields the k^{th} harmonic of the output. Let d_k be the k^{th} Fourier coefficient of the output $P_{\text{ad}}(t)$ and c_k be the k^{th} Fourier coefficient of the input $Q(t)$. Theoretically, d_k and c_k should be related as follows:

$$d_k e^{-jk\frac{2\pi}{T}t} = c_k H \left(j \frac{2\pi}{T} k \right) e^{-k\frac{2\pi}{T}t} \quad (2.26)$$

In order to validate whether the system behaves according to theory, the Fourier series coefficients of the input $Q(t)$ and those of the output $P_{\text{ad}}(t)$ were determined and the original signals were compared to the reconstructed signals from Fourier approximations using k harmonics. Figures 2-15 shows this approximation for $k = 3$.

Table 2.2 shows that the system indeed behaves in an LTI manner; the exponentials serve as eigenvectors and the Fourier coefficients are multiplied by the magnitude of the transfer function at the corresponding frequency to give the Fourier coefficients of the output, the radial pressure. We will revisit the Fourier analysis in Chapter 4.

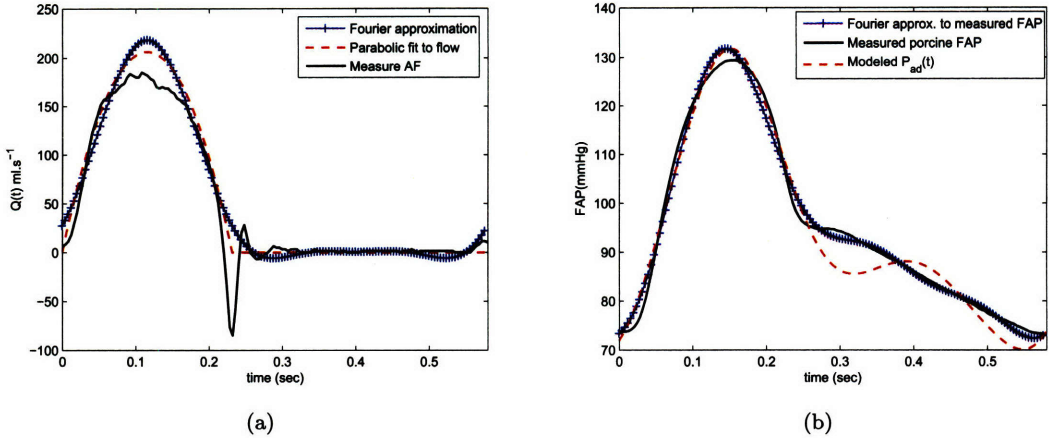


Figure 2-15: Fourier series representation up to the 3rd harmonic of a) parabolic input; b) resulting femoral pressure waveform.)

	k=0	k=1	k=2	k=3	k=4
$ c_k $	54.984	46.785	27.255	7.596	3.259
$ H $	1.814	0.280	0.250	0.082	0.030
$ c_k H $	99.741	13.100	6.814	0.623	0.098
$ d_k $	93.841	11.729	6.551	0.767	0.126

Table 2.2: Validation of the transfer function. $|H|$ was obtained using Bode plot values at specific frequencies in MATLAB.

2.6 Concluding Remarks

Though the two-element Windkessel model is a reasonable representation of the arterial tree as viewed from the left ventricle, it does not fully characterize the morphology of the pressure waveforms, which contains valuable information about parameters of the arterial tree. These parameters, if estimated, would serve as useful indices of arterial diseases. The modified Windkessel model captures in more detail three characteristics of the arterial circulation: compliances of proximal and distal arteries, resistance to flow, and blood inertance. It presents a balance between system complexity and ability to faithfully model the arterial system. In the following chapter, the parameter space of the modified Windkessel model will be analyzed before proposing an estimation scheme of arterial resistance and cardiac output.

Chapter 3

Parameter Space Analysis

In the previous chapter, we validated the modified Windkessel model as a reasonable representation of the arterial tree through forward modeling: we assumed a given functional shape for the input flow and qualitatively assessed the goodness of fit of the resulting pressure waveforms. In an ICU setting, pressures are routinely measured with minimally-to non-invasive procedures using intravenous pressure transducers or cutaneous sensors, while measurements of cardiac output require highly invasive procedures. In Chapter 1, we presented the most widely used techniques for the assessment of cardiac output in the ICU: physicians are expected to make decisions based on intermittent measurements of cardiac output via thermodilution [52]. It becomes apparent that there is high demand in the instrumentation market for a device or an algorithm which reports cardiac output continuously without the risk associated with invasive procedures. In this chapter, the parameter space of the modified Windkessel model will be analyzed in the scope of estimating cardiac output, and as many model parameters as possible, from measured pressure waveforms.

3.1 Model Parameterization

As discussed in Chapter 2, the modified Windkessel model lumps the elastic properties of the arterial tree into two compliances, C_{ad} and C_{ap} , separated by an inductor, L , and lumps the resistance to flow in the arterial tree into a total arterial resistance, R_a . The significance of the arterial compliances in the modified Windkessel model have been extensively discussed. Studies have concluded that the distal compliance, C_{ad} , could be considered as “reflective” and “oscillatory” compliance [50] and attempts to estimate it over the diastolic portion will be presented in section 3.4. The latter faced the criticism of many researchers [48] [49]: it is controversial to claim estimation of the “reflective” compliance from information in diastole when it is known that reflections are greatest during systole. Segers argued that the distal compliance has “no straightforward physical interpretation” given that his study of the “oscillatory” compliance, C_{ad} , could not attribute the distal compliance to any

specific location along the arterial tree [50].

The model as defined in Figure 2-3 also accounts for the effective downstream pressure, P_v , which can be considered as the nonzero mean circulatory pressure [44]. It is modeled as a constant pressure source which takes a nominal value of 10 mmHg in humans.

Based on our previous analysis in Section 2.4, the input flow to the modified Windkessel model is best characterized by a parabolic pulse train which has two degrees of freedom: $\beta = \frac{T}{T_s}$, the ratio of the beat duration T to the duration of the systole T_s , and Q_{\max} which was introduced earlier in Eq. 2.17. For human data sets, β can be approximated by $3\sqrt{T}$ as it has been shown that $T_s = \frac{\sqrt{T}}{3}$ [21]. However, this approximation does not hold for pigs: in our porcine data set, β is around 2.4 as seen from flow measurements.

Given the complexity of the model, many issues arise mostly from the nonlinearity of the model in the parameters. Therefore, we will first explore the sensitivity of the simulated pressure waveforms to all passive components in the circuit, R_a , C_{ad} , C_{ap} and L , as well as to the two sources in the circuit, P_v and Q_{\max} . Subsequently, we will analyze the sensitivity matrix to determine which parameters could be resolved accurately using subset selection algorithms.

Qualitative effect of each parameter on pressure waveform: Many researchers attempted to determine the specific local effect of each parameter on pressure intra beat dynamics. Segers *et al.* [50] explored the effect of each component on the morphology of the diastolic portion of radial artery pressure waveforms: they observed that the time constant of the diastolic decay is dictated by R_a and C_{ap} , while the oscillatory nature of the decay is mainly influenced by L and C_{ad} . Blood inertance, L , has the most impact on diastolic dynamics: a large L causes the diastolic portion of the beat to be damped. They also investigated the effects of pairs of parameters: higher R_a and C_{ap} yield higher end diastolic pressure, while higher C_{ad} and lower L lead to higher oscillatory characteristics. These conclusions are in line with the observations made in Section 2.5.2.1. We found that the impulse response of the modified Windkessel model had a time constant equal to the product of the total arterial compliance by the total arterial resistance. We also remarked that it had a natural frequency equal to $2\pi\sqrt{LC_{ad}}$.

3.2 Sensitivity Analysis

When performing sensitivity analysis, one is interested in measuring the effect of each of the parameters on the output, the pressure waveforms $P_{ad}(t)$ and $P_{ap}(t)$ in our case. In other words, one would like to assess the change in pressure, ΔP , resulting for a small perturbation $\Delta\theta_i$ in parameter θ_i . By performing a Taylor expansion of ΔP , one can see that a perturbation $\Delta\theta_i$ in parameter θ_i from its nominal value θ_i^o translates into a change $\frac{\partial P}{\partial\theta_i} \cdot \Delta\theta_i$ in pressure: the partial derivative $\frac{\partial P}{\partial\theta_i}$ sufficiently captures pressure waveform sensitivity with respect to parameter θ_i .

$$\Delta P(\boldsymbol{\theta}, t_j) = \frac{\partial P(\boldsymbol{\theta}, t_j)}{\partial \theta_i} \Delta \theta_i + \frac{1}{2} \frac{\partial^2 P(\boldsymbol{\theta}, t_j)}{\partial \theta_i^2} \Delta \theta_i^2 + \frac{1}{2} \frac{\partial^2 P(\boldsymbol{\theta}, t_j)}{\partial \theta_i \partial \theta_j} \Delta \theta_i \Delta \theta_j + \dots \quad (3.1)$$

As indicated in the mathematical framework of the modified Windkessel model in Section 2.3, the model is fully characterized by three differential equations, each corresponding to one of the energy storage elements. It is therefore tedious to analytically determine closed-form equations for the sensitivity of $P(\boldsymbol{\theta}, t)$ to parameter θ_i , $\frac{\partial P(\boldsymbol{\theta}, t)}{\partial \theta_i}$, where $\boldsymbol{\theta} = [\theta_1, \dots, \theta_n]$. Consequently, we approximated the partial derivative by a **two-sided finite-difference** as shown in equation (3.2).

$$\frac{\partial P(\boldsymbol{\theta}, t_j)}{\partial \theta_i} \approx \frac{P(\theta_i^0 + \Delta \theta_i; t_j) - P(\theta_i^0 - \Delta \theta_i; t_j)}{(\theta_i^0 + \Delta \theta_i) - (\theta_i^0 - \Delta \theta_i)} = \frac{P(\theta_i^0 + \Delta \theta_i; t_j) - P(\theta_i^0 - \Delta \theta_i; t_j)}{2\Delta \theta_i} \quad (3.2)$$

where $P(\theta_i^0 \pm \Delta \theta_i; t_j)$ is the resulting pressure waveform resulting for the perturbation of parameter θ_i by $\pm \Delta \theta_i$.

3.2.1 Scaling of the parameter sensitivities

Since the parameters under consideration span five dimensions, comparing the different pressure sensitivities is not straightforward. The physiological ranges of those parameters are quite different, which invalidates any relative comparison of pressure sensitivities. In order to avoid the discrepancies in their order of magnitude, a common technique is to normalize the parameter perturbation in Eq. 3.2 by the nominal values of a given parameter, except when the nominal parameter value is zero. Consequently, the sensitivity row-vector of a data point $P(t_j)$ is:

$$\left[R_a \cdot \frac{\partial P(t_j)}{\partial R_a} \quad C_{ap} \cdot \frac{\partial P(t_j)}{\partial C_{ap}} \quad Q_{max} \cdot \frac{\partial P(t_j)}{\partial Q_{max}} \quad P_v \cdot \frac{\partial P(t_j)}{\partial P_v} \quad C_{ad} \cdot \frac{\partial P(t_j)}{\partial C_{ad}} \quad L \cdot \frac{\partial P(t_j)}{\partial L} \right] \quad (3.3)$$

Also, since the pressure waveform spans a wide range of values within each beat, it might be useful to normalize the absolute change in pressure in Eq. 3.2 by the nominal pressure values along the beat. Hence, the resulting sensitivity measure becomes a measure of elasticity as defined in economics: percentage change in output for a given percentage change in a parameter.

3.2.2 Deriving the sensitivity matrix

So far, we have introduced the notion of sensitivity of a pressure data point to the given parameters. The sensitivity matrix in our context, also known as the *Jacobian*, is a compact representation of the sensitivities of the points in an entire cycle to all six parameters. Since the data sets under investigation contain both proximal and distal pressure measurements, we augment our Jacobian matrix to contain sensitivity elements of $P_{ap}^k(t)$ and $P_{ad}^k(t)$ to all six parameters. Let A_k be the augmented sensitivity matrix of the k^{th} cycle and Θ be the column scaling matrix with the nominal parameters values on the diagonal:

$$A_k \Theta = \begin{bmatrix} \frac{\partial P_{\text{ad}}(t_1)}{\partial R_a} & \frac{\partial P_{\text{ad}}(t_1)}{\partial C_{\text{ap}}} & \frac{\partial P_{\text{ad}}(t_1)}{\partial Q_{\text{max}}} & \frac{\partial P_{\text{ad}}(t_1)}{\partial P_v} & \frac{\partial P_{\text{ad}}(t_1)}{\partial C_{\text{ad}}} & \frac{\partial P_{\text{ad}}(t_1)}{\partial L} \\ \vdots & & \vdots & & \vdots & \\ \frac{\partial P_{\text{ad}}(t_N)}{\partial R_a} & \frac{\partial P_{\text{ad}}(t_N)}{\partial C_{\text{ap}}} & \frac{\partial P_{\text{ad}}(t_N)}{\partial Q_{\text{max}}} & \frac{\partial P_{\text{ad}}(t_N)}{\partial P_v} & \frac{\partial P_{\text{ad}}(t_N)}{\partial C_{\text{ad}}} & \frac{\partial P_{\text{ad}}(t_N)}{\partial L} \\ \frac{\partial P_{\text{ap}}(t_1)}{\partial R_a} & \frac{\partial P_{\text{ap}}(t_1)}{\partial C_{\text{ap}}} & \frac{\partial P_{\text{ap}}(t_1)}{\partial Q_{\text{max}}} & \frac{\partial P_{\text{ap}}(t_1)}{\partial P_v} & \frac{\partial P_{\text{ap}}(t_1)}{\partial C_{\text{ad}}} & \frac{\partial P_{\text{ap}}(t_1)}{\partial L} \\ \vdots & & \vdots & & \vdots & \\ \frac{\partial P_{\text{ap}}(t_N)}{\partial R_a} & \frac{\partial P_{\text{ap}}(t_N)}{\partial C_{\text{ap}}} & \frac{\partial P_{\text{ap}}(t_N)}{\partial Q_{\text{max}}} & \frac{\partial P_{\text{ap}}(t_N)}{\partial P_v} & \frac{\partial P_{\text{ap}}(t_N)}{\partial C_{\text{ad}}} & \frac{\partial P_{\text{ap}}(t_N)}{\partial L} \end{bmatrix} \begin{array}{c} R_a \\ C_{\text{ap}} \\ Q_{\text{max}} \\ P_v \\ C_{\text{ad}} \\ L \end{array} \quad (3.4)$$

where N represents the number of samples in each of P_{ad}^k and P_{ap}^k respectively. Each column of A_k represents the sensitivity of the entire pressure cycle to one of the parameters. This Jacobian will be revisited in Section 4.2.

The *Hessian* matrix, H , also known as the matrix of second order derivatives captures the sensitivity of $\frac{\partial P}{\partial \theta_i}$ to perturbations in θ_j . In other words, it measures the effects of changes in parameter θ_j on the pressure sensitivity to parameter θ_i . Specifically,

$$H_k \Big|_{ij} = \frac{\partial^2 P_k(t)}{\partial \theta_i \partial \theta_j} \quad (3.5)$$

The Hessian matrix is indicative of the dependency of the output on any two parameters. It becomes very useful when determining whether the parameters have separable effects on the output. If the effects are not separable, we say the sensitivity matrix is ill-conditioned, or equivalently, that the estimation or inverse problem is ill-conditioned.

3.2.3 An ill-conditioned estimation problem

Figure 3-1 shows the normalized sensitivities of proximal and distal pressure to each of the six model parameters over one cycle.

As can be seen in Figure 3-1, a radial pressure beat is not equally sensitive to all the parameters: $P_{\text{ad}}^k(t)$ is orders of magnitude more sensitive to R_a and Q_{max} , than to C_{ad} or C_{ap} . The latter observation is one indication of an ill-conditioned sensitivity matrix.

By computing the angle between each pair of sensitivity columns one can test whether two parameters affect the k^{th} cycle of the pressure waveforms in the same way. If the angle formed between two column vectors is small, it is difficult to accurately resolve any of the two underlying

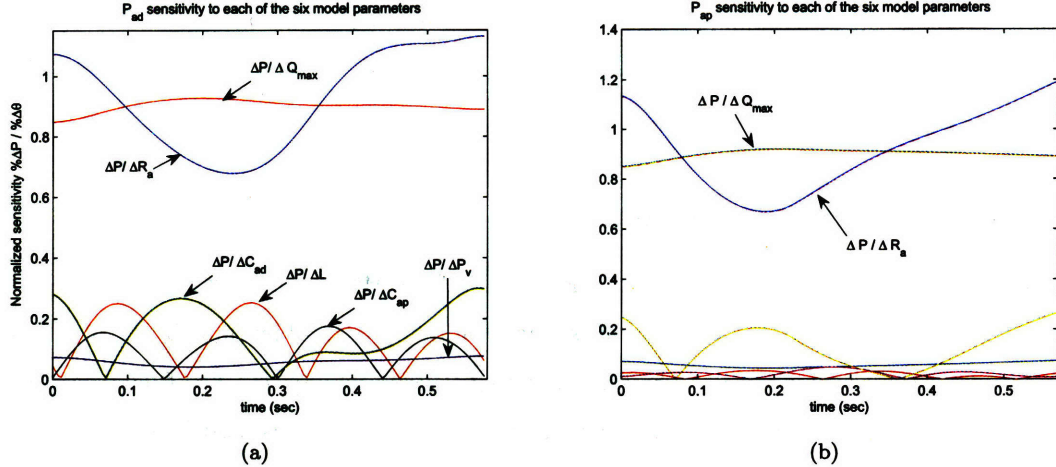


Figure 3-1: The absolute value of the columns of the sensitivity matrix of a given beat from a) the radial pressure waveform and b) the central aortic pressure waveform . Each row of the sensitivity matrix, $A_k\Theta$, is normalized by the appropriate pressure data point value so as to obtain a measure of elasticity.

	Q_{\max}	L	P_v	C_{ad}	C_{ap}
R_a	10.8	94.2	4.3	95.1	73.9
Q_{\max}	0	91.0	11.6	93.1	83.2
L	0	0	91.8	36.6	85.8
P_v	0	0	0	95.1	71.9
C_{ad}	0	0	0	0	96.6

Table 3.1: Angles between columns of the sensitivity matrix.

parameters since observed variations in pressure can be attributed to changes in either of the two parameters. Table 3.1 shows that some parameters have similar effect on radial pressure, R_a and P_v for example. This method however does not delimit which parameters could be resolved as it only considers pairs of parameters instead of the projection of all sensitivity columns onto one plane.

Another measure of ill-conditioning is to compute the 2-norm condition number of the Hessian matrix, the matrix of second order derivatives. Large condition numbers indicate that the Hessian is quasi-singular and thus the estimation problem is ill-conditioned. The 2-norm condition number of the model's Hessian matrix for some parameter values characterizing pig #5's steady state is 5.6×10^7 , reflecting an ill-conditioned estimation problem.

3.3 Subset Selection

To overcome the ill-conditioned Hessian matrix, I turn to *subset selection* developed by Velez-Reyes *et al.* [17]. Subset selection distinguishes between “weak” parameters and “strong” ones. By “weak” parameters it is meant that the output is almost insensitive to these parameters in the presence of the “strong” ones. Once the algorithm selects which parameters could be resolved accurately, the

weak parameters are fixed at nominal values which introduces some bias in the model. However, the strong parameters can be resolved robustly. The dimensionality of the sensitivity matrix is thus reduced so as to include only sensitivities to the strong parameters.

3.3.1 Subset selection algorithm

Let m be the total number of parameters in the model. If the Hessian matrix H has only ρ large eigenvalues and consequently $(m - \rho)$ small ones, then the reduced Jacobian matrix A_ρ should only include ρ fairly independent columns. The corresponding Hessian matrix, H_ρ , will then have a small condition number, reflecting good conditioning. The following procedures describes the mechanics of the algorithm [17]:

1. Let $\boldsymbol{\theta}_0$ be the parameter vector of nominal parameter values. Determine the Hessian matrix, H_0 , corresponding to the sensitivity matrix at the nominal values of the parameters.
2. Compute the SVD decomposition of H_0 : $H_0 = V\Sigma V^T$, such that the diagonal entries of Σ are in descending order.
3. By examining the magnitude of eigenvalues in Σ , determine the number of “strong” parameters, ρ .
4. Divide the matrix with the eigenvectors, V such that $V = [V_\rho \ V_{m-\rho}]$, where $V_{m-\rho}$ is the null model constructed from the last $m - \rho$ columns of V .
5. In order to determine the ρ strong parameters, compute a permutation matrix P such that, $V_\rho^T \cdot P = Q \cdot R$
6. Reorder the parameter vector according to the permutation P : $\tilde{\boldsymbol{\theta}} = P \cdot \boldsymbol{\theta}$
7. Divide the ordered parameter vector $\tilde{\boldsymbol{\theta}}$ into two vectors: $\tilde{\boldsymbol{\theta}}_\rho$ with the first ρ parameters and $\tilde{\boldsymbol{\theta}}_{m-\rho}$ which will be fixed at nominal values.

$\tilde{\boldsymbol{\theta}}_\rho$ contains the parameters which we can expect to resolve using least square estimation methods.

3.3.2 Subset selection results

For the modified Windkessel model, the SVD decomposition of H_0 results in three relatively large singular values (3.5×10^6 , 0.09×10^6 and 0.04×10^6) and three much smaller singular values (6.5×10^3 , 4.7 and 6.2×10^{-2}). Therefore, it is a reasonable choice to set ρ to 3.

Applying the resulting permutation matrix leads to an ordered parameter vector as follows: $\tilde{\boldsymbol{\theta}} = [Q_{\max} \ L \ R_a \ | \ C_{ad} \ P_v \ C_{ap}]$ where the first three parameters are to be estimated and the remaining three to be fixed at values characteristic of the physiological system. Since the blood inertance is

unlikely to vary for a given subject, we reduced our target parameter vector from three parameters to just two in order to reduce the computational overhead in computing the Jacobian:

$$\hat{\boldsymbol{\theta}}'_{\rho} = [Q_{\max} \quad R_a] \quad (3.6)$$

In the following sections, we explore previously-used techniques to approximate the parameters of the arterial tree in order to set the weak parameters at some good initial guesses.

3.4 The Uncertainty about Arterial Compliance

While the total arterial resistance could be easily obtained from measurements of cardiac output and pressure as shown in Section 3.6, researchers have been challenged with the estimation of arterial compliances. The difficulty arises from the complexity of measuring total arterial blood volume to capture variations in volume for a given variation in pressure. Researchers who took it upon themselves to study arterial compliance can be classified into two groups: those who assumed a constant compliance independent of pressure, and those who strived to capture the dependency of compliance on pressure. The assumption of a constant compliance was backed by the findings of several studies [32] [33] [38]. However, this assumption was rejected by other researchers. Liu *et al.* [44] observed, through their in-vitro experiments that a linear relationship between pressure and volume only holds for large arteries; narrow and smaller arteries impose a nonlinear P-V relationship.

In this section, we first explain five methods for the estimation of constant compliance. We then highlight some of the methods which attempt to estimate a pressure-dependent compliance.

3.4.1 Estimation of a constant compliance

Over the last century, numerous estimation schemes have been suggested for the estimation of constant compliance. However, only five methods are widely accepted. We attempt to give a concise summary on each of the following methods: the pulse pressure method, the stroke volume-to-aortic pressure ratio, the diastolic decay method, the area method, and the integral method.

3.4.1.1 The pulse pressure method [34]

The pulse pressure method (PPM) was developed by Stergiopoulos *et al.* [34] to obtain an estimate of whole-body compliance of the arterial tree. It is based on the original Windkessel model in which the capacitor represents total arterial compliance. The motivation behind using PPM was to eliminate the dependency of the estimation schemes on the morphology of the pressure waveforms as they can exhibit wave reflections which cannot be accounted for with the Windkessel model. Also, contrary to the diastolic decay method, PPM does not require zero flow in diastole which eliminates the need to know when systole ends.

This method uses measurements of blood flow and pressure at some site along the arterial tree as input to an optimization scheme. Based on the Windkessel model, arterial resistance is approximated as the ratio of mean arterial pressure and mean flow. Compliance is then adjusted according to the governing equation of the two-element Windkessel model, Eq. 2.4, so that the generated pressure waveforms by the Windkessel model with measured flow as input fit the measured pressure. The goodness of fit was determined based on the difference between the pulse pressures of the measured and generated pressure waveforms. The optimization over C_a was accomplished by simple trial-

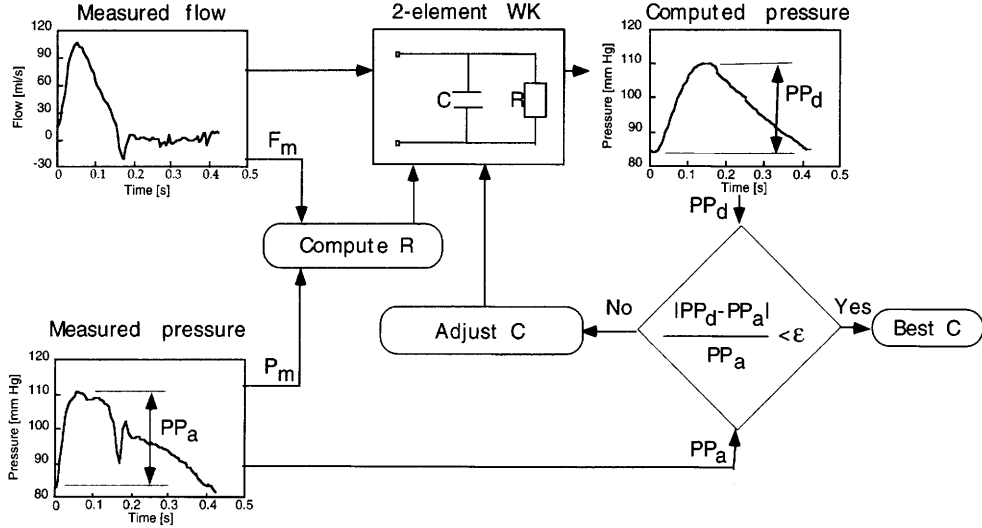


Figure 3-2: Illustrative diagram of the pulse pressure method (PPM), adapted from Stergiopoulos *et al.* [34].

and-error with the prior knowledge that large compliance values yield small pulse pressures and vice-versa. Figure 3-2 illustrates the steps of the algorithm.

A variation of the PPM was introduced by Stergiopoulos and Segers [35]. They assumed a triangular input flow reconstructed from CO (see Section 2.4) for the Windkessel model instead of the measured aortic flow. This version of the algorithm only required measurements of the radial artery pressure from which the aortic pressure waveform was generated using a generalized radial-to-aortic transfer function.

In his original paper [34], Stergiopoulos claimed that the PPM could be used to determine segmental compliance. The latter was supported by a separate study by Segers *et al.* [36] in which the PPM was compared against several methods for estimating arterial compliance. They concluded that the PPM resulted in the most accurate estimates. However, it requires a steady-state flow in order to approximate arterial resistance as the ratio of mean pressure to mean flow. This assumption does not usually hold for ICU patients.

3.4.1.2 The stroke volume-to-aortic pulse pressure ratio [40]

The approximation of arterial compliance by the ratio of stroke volume to aortic pulse pressure was initially suggested by Remington *et al.* [40]. To approximate compliance by the ratio $\frac{SV}{PP}$, one needs to assume that during systole, blood does not flow to the resistive chambers of the tree. This simplifies the governing equation of the Windkessel model (Eq. 2.4 of the two-element Windkessel)

as follows:

$$Q(t) = C_a \frac{dP(t)}{dt} \quad (3.7)$$

By integrating the above equation over the systolic phase,

$$\int_{t_0}^{t_0+T_s} Q(t) dt = C_a \int_{t_0}^{t_0+T_s} \frac{dP(t)}{dt} dt \quad (3.8)$$

one obtains

$$SV = C_a(P(t_0 + T_s) - P(t_0)) \quad (3.9)$$

As in the method discussed in Section 3.4.1.1, this method provides considerable simplicity as it only requires the magnitude of PP without any dependency on the morphology of the pressure waveform. The resulting estimate represents the compliance at mean aortic pressure, while other methods, such as the decay time method, which will be discussed in Section 3.4.1.3, determine compliance at average diastolic pressure [42]. Thus, it is expected that $\frac{SV}{PP}$ overestimates the compliance values obtained using methods such as the decay time method. It follows from this estimate,

$$R_a = \frac{MAP}{CO} = \frac{MAP}{\frac{SV}{T}} = \frac{MAP \cdot T}{PP \cdot C_a} \quad (3.10)$$

and consequently,

$$R_a \cdot C_a = \frac{MAP \cdot T}{PP} \quad (3.11)$$

Let τ be the time constant of the monoexponential diastolic decay. Then

$$\frac{T}{\tau} = \frac{PP}{MAP} \quad (3.12)$$

It is hypothesized that $\frac{T}{\tau}$ is relatively constant which maintains the ratio $\frac{PP}{MAP}$ at some constant value. The latter signifies that the higher the MAP, the larger the deviations from the mean, and consequently the larger PP is. However, the authors of the stroke volume-to-aortic pulse pressure method rejected this hypothesis based on their human data set. Researchers warned against using this approximation as an estimate of compliance as it violates the fundamental concept of the Windkessel model. There is a continuous outflow to the periphery which invalidate the assumption behind the $\frac{SV}{PP}$ method: all ejected blood stretches the large arteries during systole [25] [38]. Nevertheless, it serves as a reliable index to assess the relative change in arterial compliance.

3.4.1.3 Diastolic contour analysis [47] [52]

The method of contour analysis assumes a certain exponential solution for the model's set of differential equations which should provide a good fit to the diastolic pressure waveform. The model's

parameters are then estimated from the approximate solution. The complexity of the theoretical solution is related to the Windkessel-type model order: The higher the order of the model under investigation, the more parameters that need to be estimated. In this section, we will explore the use of this method with each of the models discussed in Section 2.

Case 1: Using the two-element Windkessel model, monoexponential fitting. The monoexponential method, also known as the *decay time method*, exploits the fact that during diastole, there is no outflow from the left ventricle to the arterial tree. Based on the original Windkessel's state-space equations during diastole,

$$\frac{dP(t)}{dt} + \frac{P(t)}{R_a C_a} = 0 \quad (3.13)$$

Solving for $P(t)$, we obtain the closed form solution for the original Windkessel during diastole:

$$P(t) = P(t_0) \cdot e^{-\frac{(t-t_0)}{R_a C_a}} \quad (3.14)$$

Since resistance is well approximated in steady state by the ratio of mean pressure to mean flow, then compliance is the only remaining unknown. The robustness of this method was questioned by Liu *et al.* [44] as they observed in their experiments that the diastolic aortic pressure does not follow an exponential decay in patients with hypertension or congestive heart failure. That said, the performance of such method can be evaluated only during steady state portions in which the diastolic phase indeed behaves like a decaying exponential function without any perturbations or artifacts.

Case 2: Using the modified Windkessel model. As mentioned in Section 2.3, the modified Windkessel model was introduced to better represent the impedance of the arterial tree at high frequencies. Watt and Burrus resolved to time-domain techniques for model identification [47]. Motivated by the validity of modeling the passive decay of the pressure levels after the closure of the aortic valve, the authors use this method as an approximation to the diastolic portion of the pressure waveform. The diastolic contour of the pressure waveform is modeled as of an exponential decay superimposed on an exponentially-damped oscillation. This representation of the pressure waveform includes six parameters which need to be estimated from the data. The closed form solution is as follows:

$$P(t) = a_1 e^{-a_2 t} + a_3 e^{-a_4 t} \cos(a_5 t - a_6) \quad (3.15)$$

Three out of the six fit parameters, a_2 , a_4 and a_5 , are dependent on the model's parameters. The remaining three parameters, a_1 , a_3 and a_6 , are related to the initial conditions of the model's state variables, $P_{ap}(0)$, $P_{ad}(0)$ and $I_l(0)$. The relationship between model parameters and the a_i 's is

presented in detail in [27] and [49]. In short,

$$C_{\text{ap}} = \frac{2a_4[(a_2 + a_4)^2 + a_5^2]}{R_a \cdot a_2(2a_4 + a_2)(a_4^2 + a_5^2)} \quad (3.16)$$

$$C_{\text{ad}} = \frac{1}{R_a \cdot (a_2 + 2a_4)} \quad (3.17)$$

$$L = \frac{R_a \cdot (a_2 + a_4)^2}{2a_4[(a_2 + a_4)^2 + a_5^2]} \quad (3.18)$$

Under the assumption that C_{ap} is much larger than C_{ad} , the relationships between the parameters of the fitting function and the model parameters simplify to [47]

$$a_2 \approx \frac{1}{R_a C_{\text{ap}}} \quad (3.19)$$

$$a_4 \approx \frac{1}{2R_a C_{\text{ad}}} \quad (3.20)$$

$$a_5 \approx \frac{1}{\sqrt{LC_{\text{ad}}}} \quad (3.21)$$

If we were to assume that resistance is estimated as the ratio of mean pressure to cardiac output, then estimating C_{ad} , C_{ap} and L becomes straightforward.

Although initial results by Goldwyn and Watt seemed promising, this method was subject to criticism by many researchers: they showed that the resulting estimates of distal compliance are not representative of the underlying variable. Burattini *et al.* [53] argued that the resolved distal compliance estimate using this method is a site dependent parameter which weakens the foundation of lumping upper body and lower distal compliances into one component.

Case 3: Using the three-element Windkessel model. In Section 2.2, we discussed the properties of the three-element Windkessel. Its ability to mimic the behavior of the arterial tree attracted many researchers who attempted to derive algorithms for the estimation of arterial parameters. Noordergraaf *et al.* [52], for example, were able to estimate arterial compliance using Fourier analysis.

In Section 2.2, we defined Z_{in} as was introduced by Noordergraaf [52]:

$$Z_{\text{in}} = Z_c + \frac{R_a}{1 + jwR_a C_a} \quad (3.22)$$

Taking the modulus and rearranging Eq. 3.22, we obtain a closed form equation for compliance C_a :

$$C_a = \frac{1}{wR_a} \sqrt{\frac{(R_a + Z_c)^2 - |Z_{\text{in}}|^2}{|Z_{\text{in}}|^2 - Z_c^2}} \quad (3.23)$$

Given measured flow and pressure, the aortic impedance spectrum can be derived for all frequencies and consequently, $|Z_{in}|$ becomes accessible. Z_c was estimated by averaging the mean of the input impedance moduli from the 2nd to the 10th harmonics [55], while R_a was approximated by the difference between $|Z_{in}(0)|$ and the calculated $|Z_c|$. Eq. 3.23 is then solved for C_a . There are many limitations to this method. One commonly discussed constraint is that the estimation schemes fails if Z_{in} is less than or equal to Z_c [55]. Also, Shim indicated that the compliance estimates could be greatly affected by wave reflections [55]. This method was further tested by Stergiopoulos *et al.* [54] in a comparison study with other methods based on the two-element Windkessel. It was concluded that compliance was strongly overestimated while the characteristic impedance, Z_c was underestimated. This model can generate better fits to pressure waveforms than the two-element methods, however it does so with inaccurate initial parameter estimates.

3.4.1.4 The area method [44]

The area method (AM) was developed in the mid 80s by Liu *et al.* [44] as an improvement to two-element Windkessel-based methods. Many researchers compared the performance of their algorithms against the area method [38]. The method was also applied to the three-element Windkessel model [54] as an attempt to refine the resultant pressure waveform fit with a more complex model.

The area method does not rely on an exponential shape of the pressure decay as do other estimation schemes such as the decay time method. Instead, it relies on the area under the pressure curve in diastole. Given that the governing equation of the Windkessel model, Eq. 2.4, is a first order differential equation, integrating both sides of the equation between two time instances in diastole, t_1 and t_2 , yields an expression in terms of point values $P(t_1)$ and $P(t_2)$ and the mean pressure over the interval $[t_1 t_2]$.

Specifically, the derivation proceeds as follows: integrating Eq. 2.4 yields

$$\int_{t_1}^{t_2} C_a \frac{dP(t)}{dt} dt + \frac{1}{R_a} \int_{t_1}^{t_2} P(t) dt = 0 \quad (3.24)$$

$$\text{where } \frac{1}{R_a} \int_{t_1}^{t_2} P(t) dt = \frac{\text{Area}_{t_1, t_2}}{R_a} \quad (3.25)$$

where the area has units of mmHg.s. To obtain mean pressure over the interval $[t_1 t_2]$, we divide the area by the difference $(t_2 - t_1)$. When t_1 is equal to the onset time, t_0 , of the beat under investigation and t_2 is equal to the time of end of diastole, t_d , the arterial resistance as defined by the Windkessel steady-state approximation can be written as $R_a = \frac{\text{MAP}}{\text{CO}}$ where MAP is

$$\text{MAP} = \frac{1}{(t_d - t_0)} \int_{t_0}^{t_d} P(t) dt = \frac{\text{Area}_{t_0, t_d}}{(t_d - t_0)} \quad (3.26)$$

For a constant compliance, independent of pressure, we obtain

$$C_a \int_{t_1}^{t_2} \frac{dP(t)}{dt} dt = C_a \cdot (P(t_2) - P(t_1)) \quad (3.27)$$

By combining Eq. 3.24, Eq. 3.25 and Eq. 3.27, the compliance can be written as a function of the area under the curve and a pressure difference according to

$$C_a = \frac{\text{Area}_{t_1, t_2}}{R_a \cdot (P(t_2) - P(t_1))} \quad (3.28)$$

where t_1 and t_2 are within the diastolic phase of the beat.

Now let $t_1 = t_s$, the time at which the dicrotic notch occurs, and $t_2 = t_d$, then the total arterial compliance can then be written as

$$C_a = \frac{\text{Area}_{t_s, t_d}}{\frac{\text{Area}_{t_0, t_d}}{\text{CO} \cdot (t_d - t_0)} \cdot (P(t_s) - P(t_d))} \quad (3.29)$$

Since cardiac output, CO, is equal to $\frac{SV}{(t_d - t_0)}$, then Eq. 3.29 can be written as

$$C_a = \frac{SV}{K(P(t_s) - P(t_d))} \quad \text{where} \quad K = \frac{\text{Area}_{t_0, t_d}}{\text{Area}_{t_s, t_d}} \quad (3.30)$$

K represents the ratio of the area under the entire beat to the area under the diastolic phase.

Segers *et al.* [25] reported that the constant compliance estimate is very sensitive to how t_d is chosen. Studies showed that the best guess for t_d would be either 28 ms after the dicrotic notch or the last 2/3 of the diastolic portion of a beat to avoid any reflections occurring at the end of systole [25], [36]. Shim *et al.* [55] remarked that the major drawback of the area method is its reliance on information in diastole, while the interaction between the characteristic impedance and the compliance is most significant during systole.

3.4.1.5 The integral method [55]

The integral method was developed by Shim *et al.* [55] as an alternative to the frequency domain method to estimate the parameters of the three-element Windkessel model. Contrary to all other methods used for the estimation of compliance in the three-element Windkessel [31] [44], it solely uses time-domain data. Most methods, originally developed for the estimation of compliance in the two-element Windkessel, were extended to the three-element Windkessel by estimating the characteristic impedance Z_c in the frequency domain – independently of the compliance – as the average of the input impedance from the 2nd to the 10th harmonic. Compliance was then determined using different time domain techniques such as the area method or the decay time method among others.

As mentioned above, the integral method is a time domain method. It differs from most of the

published methods for the estimation of C_a in that it relies on information in the early ejection stage, and does not assume any exponential form for the diastolic portion. The authors justify this approach by arguing that the interaction between the characteristic impedance, Z_c , and the compliance, C_a , is maximized right after the opening of the aortic valve when the reflected flow is negligible: in all eight dogs under investigation in their studies, the backward waveform accounted for no more than 1.4% of the measured pressure waveforms within 40 ms from ejection [55]. The characteristic impedance is obtained by averaging 6 to 8 instantaneous $\frac{PP(t_i)}{Q(t_i)}$ just after the onset of the beat. $PP(t_i)$ is the difference between pressure level at t_i and the end-diastolic pressure. Consequently,

$$Z_c = \frac{1}{N} \sum_{i=1}^N \frac{PP(t_i)}{Q(t_i)} \quad (3.31)$$

Under steady flow, total arterial resistance shadows the characteristic impedance. Hence, R_a was approximated as the ratio of mean pressure to mean flow, corrected by Z_c :

$$R_a = |Z_{in}(0)| = \frac{\text{MAP}}{\text{CO}} \quad (3.32)$$

Compliance is then estimated by integrating the governing equation of the three-element Windkessel, Eq. 2.6 given the above estimates of Z_c and R_a . Specifically,

$$\int_{t_1}^{t_2} P(t)dt + R_a C_a \int_{t_1}^{t_2} \frac{dP(t)}{dt} dt = (R_a + Z_c) \int_{t_1}^{t_2} Q(t)dt + Z_c R_a C_a \int_{t_1}^{t_2} \frac{dQ(t)}{dt} dt \quad (3.33)$$

By rearranging Eq. 3.33, a closed form for arterial compliance is derived.

$$C_a = \frac{\int_{t_1}^{t_2} P(t)dt - (R_a + Z_c) \int_{t_1}^{t_2} Q(t)dt}{R_a(P(t_1) - (t_2)) - Z_c R_a(Q(t_1) - Q(t_2))} \quad (3.34)$$

Statistical analysis of the estimated compliances of eight dogs showed that the estimates based on Eq. 3.34 differ from those obtained by the area method or the decay time method. However, the integral method estimates provided the best reconstruction of pressure waveforms for their dog data set as compared to four other methods: the area method, the diastolic decay method, the input impedance method, and an iterative nonlinear least squares method by Toorop *et al.* [46].

3.4.2 Estimation of a pressure-dependent compliance

The methods mentioned above assume that the arterial pressure-volume relationship is linear which makes the total arterial compliance of the system a constant independent of the pressure level. However, many studies concluded that the arterial pressure-volume relations of arterial segments are nonlinear [40], [41]. Otto Frank, for example, observed that using pressure-dependent compliance is one way to generalize his model [37]. It is argued in the literature that the estimated constant

compliance values are reasonably close to those calculated from a non-linear P-V relation at *normal* mean arterial pressure [38], [44]. Hence, the characterization of the pressure-volume relation is a key element in refining compliance estimates for all levels of pressure especially since, quite often, pressure waveforms exhibit high variability.

Langewouters' compliance: The most widely used form of pressure-dependent compliance is the one derived by Langewouters *et al.* [39]. It models the arterial pressure-volume curve as an arctangent. It has been used in many complex models of the cardiovascular system to characterize segmental compliance in different compartments [36]. Wesseling has incorporated Langewouter's compliance in his model-based scheme for the estimation of cardiac output [51]. Its functional form is

$$C_a^{(k)} = \frac{\alpha_1}{\alpha_2 + \alpha_3(\text{MAP}_k - P^*)^2} \quad (3.35)$$

where $C_a^{(k)}$ is the arterial compliance and MAP_k is the mean arterial pressure both for beat k . P^* represents the inflection point from the P-V relationship and is usually set at 40 mmHg. Parameters α_1 , α_2 and α_3 are patient-specific constants which can be determined from population studies [51].

Parlikar's linear compliance: Recently, Parlikar *et al.* [19] suggested a simple variation of the Langewouter's pressure-dependent compliance. They assumed a parabolic P-V relationship which yields a dynamic compliance as follows:

$$C_a^{(k)} = \beta_1 + \beta_2 \text{MAP}_k \quad (3.36)$$

where β_1 and β_2 are constants which need to be estimated. Based on their study [19], a pressure-dependent compliance improved the performance of their CO estimation scheme.

Liu's compliance based on the AM: Liu *et al.* [44] used the area method to estimate a pressure-dependent compliance for preset nonlinear pressure-volume relationship [44]. Substituting Eq. 3.25 in Eq. 3.24 gives a general form for the averaged two-element Windkessel:

$$\int_{t_1}^{t_2} C_a(P) \cdot \frac{dP(t)}{dt} dt + \frac{\text{Area}_{t_1, t_2}}{R_a} = 0 \quad (3.37)$$

In Section 2.3, compliance was defined such that $C_a(P) = \frac{dV(P)}{dP}$. By combining Eq. 2.3 and Eq. 3.37, we obtain

$$\int_{P(t_s)}^{P(t_d)} dV(P) + \frac{\text{Area}_{t_s, t_d}}{R_a} = 0 \quad (3.38)$$

Since $R_a = \frac{MAP}{CO}$ and $CO = (t_d - t_0) \cdot SV$, then

$$R_a = \frac{\text{Area}_{t_0, t_d}}{SV} \quad (3.39)$$

By substituting Eq. 3.39 in Eq. 3.38,

$$V(P(t_s)) - V(P(t_d)) = \frac{SV}{K} \quad (3.40)$$

Depending on the assumed relationship between pressure and volume, one could estimate C_a after estimating all the parameters in the volume expression as a function of pressure, $V(P(t))$.

Liu *et al.* explored three functional forms to characterize the arterial P-V relationship: exponential, logarithmic, and parabolic. For an exponential P-V curve, volume is related to pressure as follows:

$$V(t) = ae^{bP(t)} \quad (3.41)$$

where a and b are to be determined experimentally. Substituting the above equation in Eq. 3.40 results in a pressure-dependent compliance given by

$$C_a = \frac{\frac{SV}{K}be^{bP(t)}}{e^{bP(t_s)} - e^{bP(t_d)}} \quad (3.42)$$

For a logarithmic relationship, the dynamic compliance would be

$$C_a = \frac{\frac{SV}{K}}{\ln\left(\frac{P(t_s)}{P(t_d)}\right)} \quad (3.43)$$

Finally, for a parabolic relationship, the resulting compliance is similar to Eq. 3.36 proposed by Parlikar *et al.* [19]. The exponential relationship was found to be the best function as it has only one parameter independent of measurement's site, b , to be estimated by linear least-squares techniques [44]: once an estimate of b is available, the compliance estimate becomes dependent on pressure waveform characteristics and stroke volume. The parabolic function performed well on waveforms with pressures below 100 mmHg however it resulted in very poor fits for higher pressures. On the other hand, the logarithmic function behaved in the opposite way: it provides much better fits for high pressure levels.

3.5 Approximation of Blood Inertia

In the previous section, we discussed methods for estimating arterial compliance. These methods have been tested extensively in the literature. While many methods are applicable to the modified Windkessel model, the decay method as developed by Watt and Burrus [47] is the only method

which attempts to estimate the blood inertance parameter in the modified Windkessel model. The remaining methods rely on the derivation of inertance from the geometry of the vessels as described in Section 1.2.1. The accuracy of blood inertance estimates have not been given much attention as it has been argued that variations in L cannot be observed on a beat-to-beat basis, and it is also hypothesized that blood density and the length of vessels are fairly constant. Stergiopoulos *et al.* [45] evaluated segmental blood inertance in a distributed model of the arterial tree as follows:

$$L_i = \int_0^{l_s} c_u \frac{\mu}{A_i} dx \quad (3.44)$$

where L_i is the blood inertance in vessel i , A_i is the cross sectional area, μ is the blood density, and c_u is the velocity profile coefficient [45]. We did not attempt to estimate L in our CO estimation scheme, something we explained earlier in this chapter.

3.6 Previous Estimation Methods of Resistance

As presented in Section 1.2.1, R_a in Windkessel-type models is approximated in practice using Ohm's law [8] [34] [35] [45] [47] [50] [51] [55]. While Poisseuille's law highlights the dependence of arterial resistance on the geometry of the vessels, resistance as defined in Windkessel-type can be estimated solely from steady state data where compliance and inertance have no effect. Under Ohm's law, resistance is equal to the ratio of mean arterial pressure to mean flow.

Under transient behavior, Toorop *et al.* [46] accounted for the compliance effects in the three-element Windkessel by subtracting from mean flow the blood flow which is held by the arterial compliance. Specifically,

$$R_{\text{transient}} = \frac{\text{MAP}_k}{\text{CO}_k - \frac{\Delta P_k C_k}{T_k}} \quad (3.45)$$

Parlikar *et al.* [19] relied on beat-to-beat least squares estimates of the time constant τ_k of the Windkessel model ($\tau_k = R_a^{(k)} C_a^{(k)}$) and estimates of compliance according to Eq. 3.36 to obtain a beat-to-beat estimate of R_a in the simple Windkessel model.

3.7 Concluding Remarks

In this chapter, we analyzed the parameter space of the modified Windkessel model in order to better understand the inverse problem which is explained in detail in the next chapter. Using the subset selection algorithm, we determined that we can reliably estimate two of the modified Windkessel model parameters, R_a and Q_{\max} . A review of previously developed methods for the estimation of arterial compliance and blood inertance in Windkessel-type models was also presented.

In the following chapter, the inverse or estimation problem for cardiac output and arterial re-

sistance will be discussed, and a scheme for fixing the other parameters in the modified Windkessel model will presented.

Chapter 4

Beat-by-beat Parameter Estimation

In Chapter 2, we introduced the modified Windkessel model as a faithful representation of the arterial tree. In Chapter 3, we further expanded the mathematical framework of the modified Windkessel model by exploring the model's parameter space and its effect on the pressure waveforms. We also presented a literature review of previous methods for the estimation of three key physiologic parameters: the arterial compliance, peripheral resistance, and blood inertance.

In this chapter, we analyze the inverse problem for the estimation of cardiac output. We will discuss our approach to estimate cardiac output and arterial resistance reliably from pressure waveforms using a nonlinear least squares (NLLS) routine. To do so, we first highlight the nonlinearity of the model in the parameters under investigation, R_a and Q_{\max} . We then discuss key concepts of NLLS optimization techniques before concluding with our beat-by-beat estimation scheme.

4.1 Nonlinear Dependence of Blood Pressure on R_a and Q_{\max}

In Section 3.3, the application of the subset selection algorithm developed by Velez-Reyes et al. [17] resulted in a reduced parameter vector comprising the total arterial resistance, R_a , and the maximum blood outflow of the left ventricle when modeled as a parabola, Q_{\max} . According to our parameter space analysis in Chapter 3, the sensitivity column vectors corresponding to R_a and Q_{\max} are almost collinear: the angle formed by the two vectors is around 10° . The absence of orthogonality between the two sensitivity vectors suggests that it would be hard to separate the effect of R_a on pressure from that of Q_{\max} . However, subset selection suggests that a NLLS approach would be able to accurately estimate Q_{\max} , L , and R_a .

In Chapter 2, we concluded that blood outflow of the left ventricle is best modeled as a parabolic

pulse train of variable periodicity. Specifically,

$$Q(t) = \sum_k \left(a(t - t_k)^2 + b(t - t_k) \right) \left(u(t - t_k) - u(t - (t_k + T_s)) \right) \quad (4.1)$$

where

$$a = \frac{-6 \cdot SV_k}{T_s^3} \quad b = \frac{6 \cdot SV_k}{T_s^2} \quad (4.2)$$

Under the above assumption, the interaction between Q_{\max} and R_a could be explicitly seen in the steady state equation of the modified Windkessel model:

$$R_a = \frac{\text{MAP}_k}{\text{CO}_k} = \frac{\text{MAP}_k}{\frac{2}{3\beta_k} Q_{\max}} \quad (4.3)$$

where $\beta_k = \frac{T_k}{T_s}$.

It can be inferred from Eq. 4.3 that an increase in mean pressure could be due to either an increase in arterial resistance for a constant flow or an increase in cardiac output for constant resistance.

Based on the state space representation of the model in Eq. 2.10, the pressure waveforms are nonlinearly dependent on R_a and Q_{\max} . Substituting Eq. 2.7 in Eq. 2.9 results in the Kirchhoff current law equation at the supernode consisting of the inductor:

$$Q(t) = C_{ap} \frac{dP_{ap}(t)}{dt} + C_{ad} \frac{dP_{ad}(t)}{dt} + \frac{P_{ad}(t)}{R_a} \quad (4.4)$$

If we express $P_{ap}(t)$ in terms of $P_{ad}(t)$ and its derivatives and we model blood flow as a parabolic function in systole, then Eq. 4.4 can be written as

$$R_a L C_{ad} C_{ap} \frac{d^3 P_{ad}(t)}{dt^3} + L C_{ap} \frac{d^2 P_{ad}(t)}{dt^2} + R_a (C_{ad} + C_{ap}) \frac{dP_{ad}(t)}{dt} + P_{ad}(t) = R_a Q_{\max} \left(\frac{-4t^2}{T_s^2} + \frac{4t}{T_s} \right) (u(t) - u(t - T_s)) \quad (4.5)$$

The above differential equation is nonlinear in the parameters. Hence, estimates of the parameters R_a and Q_{\max} could only be resolved using NLLS optimization methods. Most well established methods are based on the Gauss-Newton approximation which is presented in Section 4.2.2.

4.1.1 Problem statement

The objective of our project is to estimate cardiac output and arterial resistance from arterial pressure waveforms. We aim to extract as much information as possible from measured proximal and distal pressure waveforms to approximate cardiac output. In an ICU setting, femoral or radial pressures are routinely recorded to monitor a patient's hemodynamic state. For the porcine data set used in Chapter 5, waveforms of both central aortic pressure and femoral artery pressure are used

in the inverse problem to estimate model's parameters. That is,

$$\mathbf{P}_{\text{measured}}^T = \begin{bmatrix} P_{\text{ap}}(t_1) & \dots & P_{\text{ap}}(t_N) & P_{\text{ad}}(t_1) & \dots & P_{\text{ad}}(t_N) \end{bmatrix} \quad (4.6)$$

where N is the number of data points in the k^{th} cycle in each of the pressure waveforms, $P_{\text{ad}}(t)$ and $P_{\text{ap}}(t)$. We defined $\boldsymbol{\theta}$ as the parameter vector of the modified Windkessel model. We wish to find the set of parameters which leads to best fits of the measured waveforms. Assuming we have good guesses for C_{ad} , C_{ap} , and L , we aim to obtain beat-by-beat estimates of the optimal arterial resistance, R_a and maximum blood flow, Q_{max} , by comparing the output pressure waveforms of the modified Windkessel model to $\mathbf{P}_{\text{measured}}$. By estimating these two parameters, we obtain a reliable estimate of CO in two different ways. Cardiac output's relation to R_a could be determined from the model's steady state equation:

$$\widehat{\text{CO}}_k = \frac{\text{MAP}_k}{\widehat{R}_a} \quad (4.7)$$

Its relation to Q_{max} could be obtained from the parabolic flow equation:

$$\widehat{\text{CO}}_k = \frac{2}{3\beta} \cdot \widehat{Q}_{\text{max}} \quad \text{where } \beta = \frac{T}{T_s} \quad (4.8)$$

4.2 Nonlinear Least Squares Optimization Over One Cardiac Cycle

In this section, we will derive the parameter update equation resulting from NLLS optimization for pressure waveforms in an individual cardiac cycle. We will account for column-scaled Jacobian matrices and weighted residual vectors in the derivation below. Although the method of least-squares is one of the most commonly used estimation techniques, there are many tuning aspects to the nonlinear version of the algorithm. First, we will explain the theory behind least-squares followed by the derivation of the Gauss-Newton NLLS optimization. Subsequently, we will introduce a particular regularization technique known as the Levenberg-Marquardt algorithm.

4.2.1 Cost functions

Typically in estimation algorithms, the cost function to be minimized is a function of the estimation error, the difference between the model's output and the measured data. Least-squares solutions are obtained by minimizing, sometimes a weighted version of, the sum of squares of the prediction error. Let $\mathbf{r}(\hat{\boldsymbol{\theta}})$ be the prediction error between the model's pressure waveforms and the measured data, specifically, $\mathbf{r}(\hat{\boldsymbol{\theta}}) = \mathbf{P}_{\text{measured}} - \mathbf{P}(\hat{\boldsymbol{\theta}}, t)$. Note that $\mathbf{P}(\hat{\boldsymbol{\theta}}, t)$ is the column-vector containing samples of model-generated proximal and distal pressures for some $\hat{\boldsymbol{\theta}}$. The cost function to be minimized

can be written in terms of r as follows:

$$\Phi(\boldsymbol{\theta}) = \frac{1}{2} \mathbf{r}^T W \mathbf{r} \quad (4.9)$$

where W is a diagonal matrix of weights. The least squares solution, $\boldsymbol{\theta}^{LS}$, can then be expressed as follows:

$$\boldsymbol{\theta}^{LS} = \arg \min_{\boldsymbol{\theta}} \frac{1}{2} \sum_{i=1}^{2N} w_i r_i^2(\boldsymbol{\theta}) \quad (4.10)$$

where w_i represents the weight associated with the squared error at the i^{th} data point of $\mathbf{P}(\boldsymbol{\theta}, t)$. The weight factor w_i is usually associated with the uncertainty about data point i . It plays an important role in the estimation algorithm as it allows the more reliable data points to be used preferentially in determining the estimates of the parameters. *Statistical weighting*, for example, uses the inverse of the variance of data point i of $\mathbf{P}(\boldsymbol{\theta}, t)$ as the weight:

$$w_i = \frac{1}{\sigma_i^2} \quad (4.11)$$

In cases in which we cannot assess the uncertainty about the prediction error of the i^{th} data point, we simply assume the uncertainty about all points to be the same. This leads to *unit weighting* i.e. $w_i = 1$.

If we were to determine the uncertainty for our data set, one possible scheme to compute variances is to stack all steady state beats and to derive distributions around each data point (normalized histograms). We could also benefit from prior belief about the model's ability to represent the data: if we believe our model captures the systolic dynamics better than the diastolic ones, then we could assume higher prediction variance in diastole leading to smaller weights for the diastolic portion of the cardiac cycle.

4.2.2 Gauss–Newton nonlinear least squares optimization

The NLLS estimation scheme attempts to find the effect of a normalized perturbation, $\Delta\% \boldsymbol{\theta}$, around $\boldsymbol{\theta}^0$ on the pressure waveforms. The derivation of the scheme proceeds as follows:

$$\Delta P = \left[A\Theta \right]_{\boldsymbol{\theta}^0} \cdot \Delta\% \boldsymbol{\theta} = \mathbf{r}(\boldsymbol{\theta}^0) \quad (4.12)$$

where $\Delta\% \boldsymbol{\theta} = \Theta^{-1} \Delta \boldsymbol{\theta} = \Theta^{-1} (\boldsymbol{\theta}^1 - \boldsymbol{\theta}^0)$. In Section 3.2.2, we defined the matrix of the first derivatives, A , as the Jacobian matrix which we scaled by Θ , the column-scaling matrix of nominal parameter values. We also defined the matrix of second derivatives, H , as the Hessian matrix. The inverse model aims to determine the values of the parameters in $\boldsymbol{\theta}$ for a given pressure waveform. In the previous section, we saw that the least-squares solution does this by minimizing the weighted sum

of squares of the prediction errors, as shown in Eq. 4.10.

Deriving the least squares solution: Let $\boldsymbol{\theta}^0$ be the vector of initial guesses of the parameters and $\boldsymbol{\theta}^1$ be an estimate of the parameter vector. Given our initial guess, $\boldsymbol{\theta}^0$, we could approximate the cost function in Eq. 4.10 by its Taylor approximation around $\boldsymbol{\theta}^0$:

$$\Phi(\boldsymbol{\theta}) = \Phi(\boldsymbol{\theta}^0) + \left[\frac{\partial \Phi}{\partial \boldsymbol{\theta}} \right]_{\boldsymbol{\theta}^0} \Delta_{\%} \boldsymbol{\theta} + \frac{1}{2} \Delta_{\%} \boldsymbol{\theta}^T \left[\frac{\partial^2 \Phi}{\partial \boldsymbol{\theta}^2} \right]_{\boldsymbol{\theta}^0} \Delta_{\%} \boldsymbol{\theta} \quad (4.13)$$

We then aim to minimize $\Phi(\boldsymbol{\theta})$ with respect to $\Delta_{\%} \boldsymbol{\theta}$. To do so, we differentiate the objective function with respect to $\Delta_{\%} \boldsymbol{\theta}$ and set it to zero. The latter leads to the following equation:

$$\left[\frac{\partial \Phi}{\partial \boldsymbol{\theta}} \right]_{\boldsymbol{\theta}^0} + \left[\frac{\partial^2 \Phi}{\partial \boldsymbol{\theta}^2} \right]_{\boldsymbol{\theta}^0} \Delta_{\%} \boldsymbol{\theta} = 0 \quad (4.14)$$

Rearranging Eq. 4.14 under the assumption that the Hessian matrix, $H = [\partial^2 \Phi / \partial \boldsymbol{\theta}^2]_{\boldsymbol{\theta}^0}$, is non-singular, yields the following least squares solution:

$$\Delta_{\%} \boldsymbol{\theta} = - \left[\frac{\partial^2 \Phi}{\partial \boldsymbol{\theta}^2} \right]_{\boldsymbol{\theta}^0}^{-1} \left[\frac{\partial \Phi}{\partial \boldsymbol{\theta}} \right]_{\boldsymbol{\theta}^0} \quad (4.15)$$

The matrix of first-order derivatives in Eq. 4.15 relates the sensitivity matrix to the parameter vector $\boldsymbol{\theta}$ as follows:

$$\left[\frac{\partial \Phi}{\partial \boldsymbol{\theta}} \right]_{\boldsymbol{\theta}^0} = (\sqrt{W} A \Theta)^T \sqrt{W} \mathbf{r}(\boldsymbol{\theta}) \Big|_{\boldsymbol{\theta}^0} \quad (4.16)$$

The Gauss-Newton approximation of the Hessian matrix: The matrix of second-order derivatives in Eq. 4.15 can be obtained by differentiating Eq. 4.16 with respect to $\boldsymbol{\theta}$. Using the chain rule, the $(i, j)^{\text{th}}$ entry of $[\partial^2 \Phi / \partial \theta_i \partial \theta_j]_{\boldsymbol{\theta}^0}$ can be written as

$$H_{ij} = \frac{\partial^2 \Phi}{\partial \theta_i \partial \theta_j} = (\Theta A^T W A \Theta)_{ij} + g(W, \mathbf{r}, \boldsymbol{\theta}) \quad (4.17)$$

Where $g(W, \mathbf{r}, \boldsymbol{\theta})$ is a function of the second derivative of the residuals with respect to the i^{th} and j^{th} parameters. The Gauss-Newton approximation ignores $g(W, \mathbf{r}, \boldsymbol{\theta})$ as it is negligible for small residuals. This leads to an approximation of the Hessian given by:

$$H \approx \Theta A^T W A \Theta \approx (\sqrt{W} A \Theta)^T (\sqrt{W} A \Theta) \quad (4.18)$$

The NLLS parameter update equation: If we apply the Gauss-Newton approximation of the Hessian matrix, Eq. 4.15 can be rewritten:

$$\Delta_{\%} \boldsymbol{\theta} = -[(\sqrt{W} A \Theta)^T (\sqrt{W} A \Theta)]^{-1} (\sqrt{W} A \Theta)^T \sqrt{W} \mathbf{r}(\boldsymbol{\theta}) \quad (4.19)$$

When the dependent variable, $\mathbf{P}(\boldsymbol{\theta}, t)$, is a linear function of the parameters, $\boldsymbol{\theta}^1 = \boldsymbol{\theta}^{LS}$, unless the Hessian matrix is ill-conditioned. However, when $\mathbf{P}(\boldsymbol{\theta}, t)$ is nonlinear in the parameters, an iterative process is required. As was indicated in Section 4.1, the modified Windkessel model is nonlinear in the two strong parameters, and thus the NLLS solution must be obtained.

The Gauss-Newton approximation also transforms the NLLS estimation problem into a series of linear least squares estimation problems. At each iteration, a parameter update vector is generated by minimizing the cost function described above. The NLLS update equation at the end of iteration i is the following:

$$\boldsymbol{\theta}^{i+1} = \boldsymbol{\theta}^i - \boldsymbol{\Theta}[(\sqrt{W}A\boldsymbol{\Theta})^T(\sqrt{W}A\boldsymbol{\Theta})]^{-1}(\sqrt{W}A\boldsymbol{\Theta})^T\sqrt{W}\mathbf{r}(\boldsymbol{\theta}^i) \quad (4.20)$$

Parameter vector $\boldsymbol{\theta}^{i+1}$ is considered an improved estimate of $\boldsymbol{\theta}$ if it yields a better fit to the data, in other words, if $\Phi(\boldsymbol{\theta}^{i+1}) < \Phi(\boldsymbol{\theta}^i)$. Note that if A is a full-rank matrix, then W is a positive definite symmetric matrix representing the weight matrix, and the iterative scheme converges to $\boldsymbol{\theta}^{LS}$.

Tikhonov regularization: There are many efficient NLLS algorithms which involve regularization techniques to overcome ill-conditioned Hessian matrices which are characterized by a large condition number, the ratio of its largest singular value of a matrix to its smallest. The most commonly used method is the Tikhonov regularization which constrains the magnitude of the term, $\|\Delta_{\%}\boldsymbol{\theta}\|$. The optimization problem thus becomes

$$\boldsymbol{\theta}^{LS} = \arg \min_{\boldsymbol{\theta}} \left(\Phi(\boldsymbol{\theta}) + \epsilon^2 \|\Delta_{\%}\boldsymbol{\theta}\|^2 \right) \quad (4.21)$$

where ϵ^2 is called the *Tikhonov factor*, a damping variable to suppress small eigenvalues of the H . By reducing the condition number of H , the least squares solution becomes more stable, i.e., the Hessian matrix is no longer quasi-singular. This constrained optimization problem in Eq. 4.21 has an explicit solution:

$$\Delta_{\%}\boldsymbol{\theta} = [(\sqrt{W}A\boldsymbol{\Theta})^T(\sqrt{W}A\boldsymbol{\Theta}) + \epsilon^2 I]^{-1}(\sqrt{W}A\boldsymbol{\Theta})^T\sqrt{W}\mathbf{r}(\boldsymbol{\theta}) \quad (4.22)$$

The Tikhonov factor can be set arbitrarily. However, if it is too large, it makes the iterative NLLS process extremely slow as the update vector, $\boldsymbol{\theta}^{i+1}$, satisfying the cost function in Eq. 4.21 is dominated by the large term, $\epsilon^2 \|\Delta_{\%}\boldsymbol{\theta}\|^2$. Numerous schemes have been developed to dynamically adjust ϵ^2 so that the conditioning of the Hessian is improved with minimal computational overhead. In the following section, we will explore the Levenberg-Marquardt algorithm for adjusting the Tikhonov factor.

4.2.3 Levenberg-Marquardt algorithm

The Levenberg-Marquardt (LM) algorithm is a systematic method for adjusting the damping factor, ϵ^2 , depending on how $\Phi(\boldsymbol{\theta}^{i+1})$ compares to $\Phi(\boldsymbol{\theta}^i)$. The LM algorithm provides a solution to Eq. 4.21 by behaving like a gradient-descent algorithm for large ϵ^2 , or like the Gauss-Newton algorithm, derived in Section 4.2.2, for small ϵ^2 . On one hand, a large ϵ^2 requires that the magnitude of parameter updates to be small in order to satisfy the minimization problem. This yields small increments at each step in the iterative NLLS scheme. On the other hand, when ϵ^2 is small, $\boldsymbol{\theta}$ is mainly influenced by the magnitude of $\Phi(\boldsymbol{\theta})$, which leads to the Gauss-Newton NLLS solution.

The intuition behind the LM algorithm is that when the prediction error is large, the solution at the current iteration is distant from the optimal one, and hence, a gradient-descent approach would broadly guide the iterative process towards the solution. However, when the prediction error becomes relatively small, the LM algorithm decreases the regularization factor to take advantage of the computational efficiency of the Gauss-Newton algorithm.

The LM algorithm has three degrees of freedom: the initial value of the damping factor, ϵ^2 , a divisor, γ , which is used to scale down ϵ^2 when moving towards the optimal solution, and a multiplier, α , which scales up ϵ^2 when moving away from the optimum. The multiplier has to be smaller than the divisor so that the more iterations we do, the closer the solution will get to the correct solution. Those two tuning parameters allow the LM algorithm to dynamically adjust its behavior between a typical gradient-descent algorithm and the Gauss-Newton algorithm.

In order to assess whether we are getting closer to the optimal solution at the end of the i^{th} iteration, We use the root mean squared error, RMSE_i , which will be discussed in more detail in Section 4.2.4, instead of $\Phi(\boldsymbol{\theta})$. If RMSE_{i+1} is less than RMSE_i , then the parameter estimates are closer to the optimal solution along the error curve, and consequently, a smaller damping factor ϵ^2 is needed at the next iteration: $\epsilon_{i+1}^2 = \epsilon_i^2 / \gamma$, where $\gamma > 1$. If however, RMSE_{i+1} is larger than RMSE_i , the new estimates is further away from the correct solution which necessitates a larger damping at the next iteration: $\epsilon_{i+1}^2 = \alpha \cdot \epsilon_i^2$, where $\alpha > 1$.

4.2.4 Goodness-of-fit

Goodness-of-fit determines how well a mathematical model matches the underlying data. There are several metrics which could be used to quantify the discrepancies between two waveforms. In our scheme, we use the root mean squared error (RMSE) as the similarity metric between the resulting pressure waveforms for a given set of parameters, $\boldsymbol{\theta}$ and the measured $P_{\text{ad}}(t)$ and $P_{\text{ap}}(t)$.

$$\text{RMSE}(\hat{\boldsymbol{\theta}}) = \sqrt{\frac{\mathbf{r}^T W \mathbf{r}}{2N}} \quad (4.23)$$

where $2N$ is the number of samples used to assess the fit. Intuitively, the error at each sample is about RMSE mmHg on average. If W is the weighting matrix discussed previously, then this metric is called *root mean squared relative error* as the error at each data point is weighed by the inverse of the uncertainty about that point [56]. These metrics are used in the estimation scheme as part of the Levenberg-Marquardt algorithm, i.e., the RMSE between a model's pressure waveforms and measured pressure waveforms dictates whether the damping factor should be larger or smaller during the next iteration.

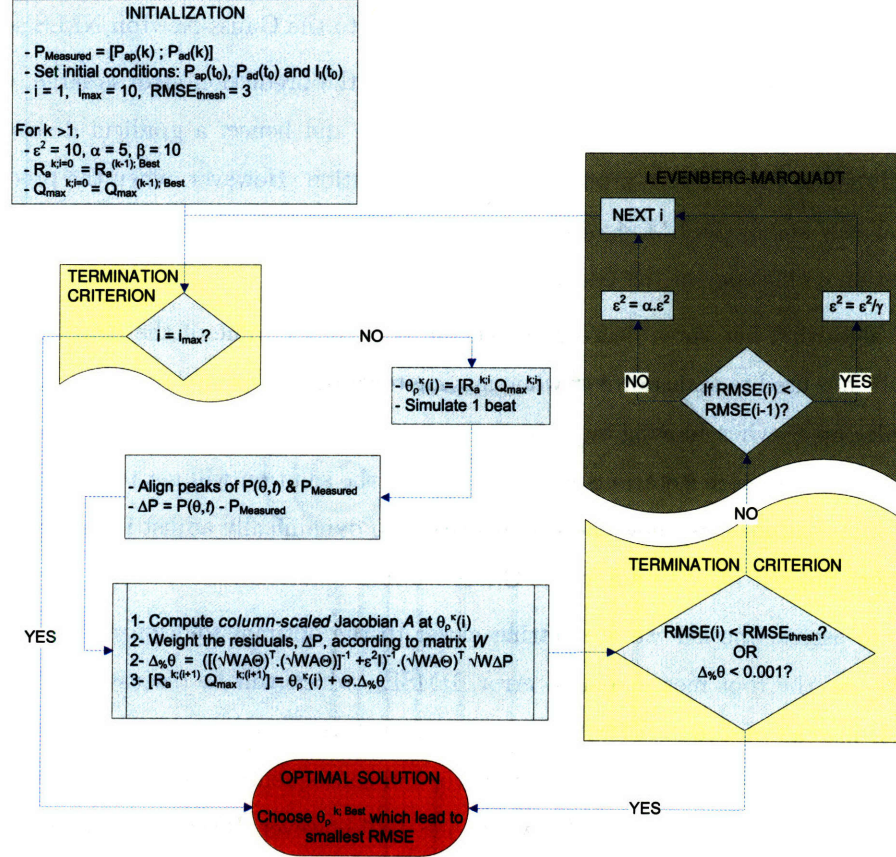


Figure 4-1: NLLS estimation scheme over one heart cycle.

4.3 Continuous Beat-by-Beat Estimation

So far, we discussed the mathematical framework of the parameter estimation scheme over *one cycle* which is summarized in Figure 4-1. Our goal is to obtain beat-by-beat estimates of arterial resistance and cardiac output from pressure waveforms. We first need to detect the onset of each cardiac cycle so we can apply the estimation algorithm. There are some major challenges in developing our estimation scheme: the choice of initial conditions for the state variables, the nominal values of the “weak” parameters and the initial guess of the parameters in θ . In this section we highlight the solution to each challenge before we summarize the details of the beat-by-beat estimation algorithm.

4.3.1 Setting the initial conditions of state space variables

The choice of initial guesses of state variables plays an important role in the convergence and the efficiency of the algorithm. In Eq. 2.10, we described the modified Windkessel model using three state variables: $P_{\text{ap}}(t)$, $P_{\text{ad}}(t)$, and $I_l(t)$. Given that the Jacobian is derived using a two-sided finite difference approximation, it is crucial to choose good initial guesses for the state variables so that the number of simulated cycles can be kept at a minimum.

Specifically, for each cycle k , let $P_{\text{ap}}^k(t)$ and $P_{\text{ad}}^k(t)$ be the measured pressure waveforms at the aorta and the femoral artery respectively. Then, the guesses for initial conditions of $\widehat{P}_{\text{ap}}(t)$ and $\widehat{P}_{\text{ad}}(t)$ would be $P_{\text{ap}}^k(t_0)$ and $P_{\text{ad}}^k(t_0)$ respectively. The initial current through the inductor, $I_l^k(t_0)$, can be approximated by rearranging the first equation from the state space model in Eq. 2.10 at $t = t_0$:

$$I_l^k(t_0) = C_{\text{ap}} \cdot \frac{dP_{\text{ap}}^k(t_0)}{dt} + Q(t_0) \quad (4.24)$$

Since the flow $Q(t)$ is modeled as a parabola in systole and is zero at $t = t_0$, $I_l^k(t_0)$ is equal to $C_{\text{ap}} \frac{dP_{\text{ap}}^k(t_0)}{dt}$. As long as the measured pressure waveforms are not too noisy, a good guess of $I_l^k(0)$ can be obtained as the product of C_{ap} by the slope at $t = t_0$ of the pressure waveform. Figure 4-2 illustrates how the values of the initial conditions are determined from measured pressure waveforms.

4.3.2 Setting C_{ap} , C_{ad} and L

We initially characterized the MWK model with four passive components and two sources, a total of six parameters. Subsequently, subset selection allowed us to reduce the parameter vector to one consisting of R_a and Q_{\max} . The remaining parameters need to be set at some nominal values which allow good fits to the pressure waveforms. In Section 3.4, we described previous methods for estimating arterial compliance in Windkessel-type models. We could be tempted to implement any of the methods to determine the nominal values of C_{ad} and C_{ap} . However, almost all the methods

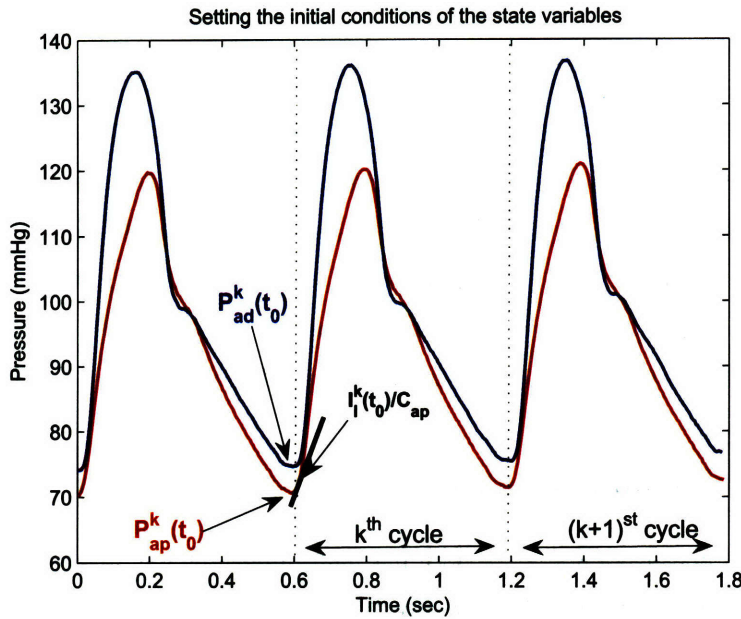


Figure 4-2: Setting the initial conditions for the state variables of the model.

assume blood flow as a given variable, defeating our estimation goal. Therefore, we explored two possible schemes which only require one measurement or estimate of cardiac output.

Grid search over C_{ap} , C_{ad} , and L : The simplest scheme consists of implementing a grid search over physiological ranges inferred from in vivo studies of the three variables, C_{ap} , C_{ad} , and L . Given that blood inertance variations are much slower than variations in arterial compliance, we perform a coarse search over the range of L and a fine search over the ranges of C_{ap} and C_{ad} . Having measured or estimated cardiac output over the first beat, R_a , and Q_{max} are then accurately set as described earlier. Hence, for every combination $[C_{ap}(i) ; C_{ad}(i) ; L(i)]$, the RMSE between the generated pressure cycle and the initial measured beat is used to determine the goodness-of-fit. The set of weak parameters which yields the smallest RMSE is then chosen to be the nominal values for the arterial compliances and the blood inertance.

Figure 4-3 shows one possible implementation of the grid search over four different values of L and 40 values for each of the compliances, 4×40^2 different combinations. This figure uses data from one of the pigs in the porcine data set described in the next chapter.

Linear least squares approach: An alternative approach to setting C_{ap} , C_{ad} , and L using a grid search is to exploit the information in the proximal and distal pressure waveforms through the input-output equation of the model. We previously derived the input-output relation for our model

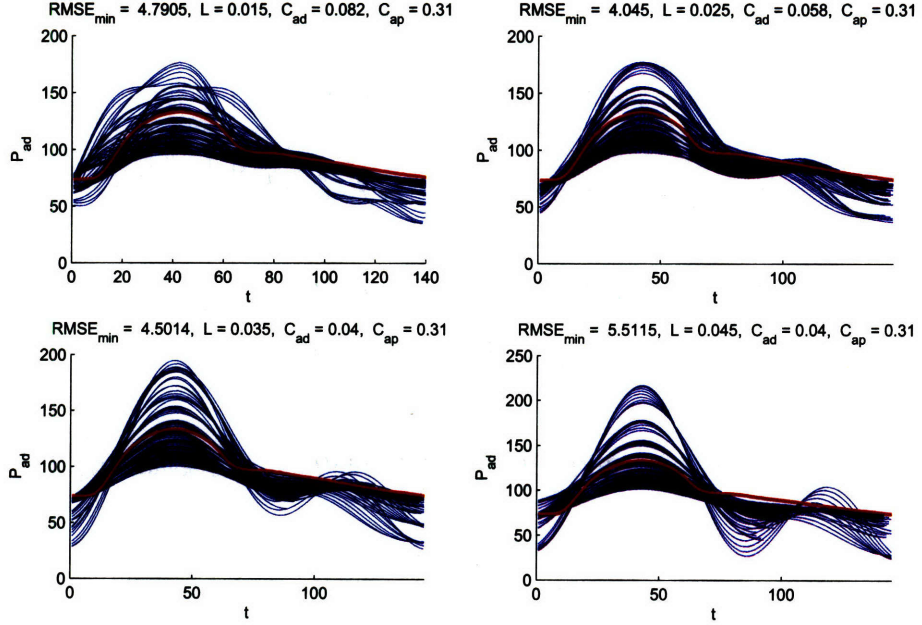


Figure 4-3: Grid search over the weak parameters for Pig #5.

to obtain the following equation:

$$C_{\text{ap}} \frac{dP_{\text{ap}}(t)}{dt} + C_{\text{ad}} \frac{dP_{\text{ad}}(t)}{dt} + \frac{P_{\text{ad}}(t)}{R_a} = Q(t) \quad (4.25)$$

Integrating Eq. 4.25 between t_1 and t_2 yields the following equation:

$$C_{\text{ap}} \left(P_{\text{ap}}(t_2) - P_{\text{ap}}(t_1) \right) + C_{\text{ad}} \left(P_{\text{ad}}(t_2) - P_{\text{ad}}(t_1) \right) + \frac{1}{R_a} \int_{t_1}^{t_2} P_{\text{ad}}(t) dt = \int_{t_1}^{t_2} Q(t) dt \quad (4.26)$$

We can rewrite an intra-beat version of Eq. 4.26, under the assumption of a parabolic pulse train as blood flow, by integrating between two intra-beat time instances, t_1 and t_2 , as follows:

$$\begin{aligned} C_{\text{ap}} \left(P_{\text{ap}}(t_2) - P_{\text{ap}}(t_1) \right) + C_{\text{ad}} \left(P_{\text{ad}}(t_2) - P_{\text{ad}}(t_1) \right) + \frac{t_2 - t_1}{R_a} < P_{\text{ad}}(t) >_{t_1}^{t_2} = \\ \left(\frac{a}{3} \min(t_2, T_s)^3 + \frac{b}{2} \min(t_2, T_s)^2 \right) - \left(\frac{a}{3} \min(t_1, T_s)^3 + \frac{b}{2} \min(t_1, T_s)^2 \right) \end{aligned} \quad (4.27)$$

where $< P_{\text{ad}}(t) >_{t_1}^{t_2}$ denotes the average of P_{ad} on the interval $[t_1; t_2]$. This equation is linear in C_{ap} , C_{ad} , and $\frac{1}{R_a}$. Hence, if we pick a few (t_i, t_j) pairs within the first beat, $0 < t_i, t_j < T_1$, we can set

up a linear least-squares (LS) problem over samples from the first measured beat:

$$\begin{bmatrix} P_{\text{ap}}(t_{j_1}) - P_{\text{ap}}(t_{i_1}) & P_{\text{ad}}(t_{j_1}) - P_{\text{ad}}(t_{i_1}) & (t_{j_1} - t_{i_1}) < P_{\text{ad}}(t) >_{t_{i_1}}^{t_{j_1}} \\ \cdot & \cdot & \cdot \\ P_{\text{ap}}(t_{j_n}) - P_{\text{ap}}(t_{i_n}) & P_{\text{ad}}(t_{j_n}) - P_{\text{ad}}(t_{i_n}) & (t_{j_n} - t_{i_n}) < P_{\text{ad}}(t) >_{t_{i_n}}^{t_{j_n}} \\ \cdot & \cdot & \cdot \\ P_{\text{ap}}(t_{j_z}) - P_{\text{ap}}(t_{i_z}) & P_{\text{ad}}(t_{j_z}) - P_{\text{ad}}(t_{i_z}) & (t_{j_z} - t_{i_z}) < P_{\text{ad}}(t) >_{t_{i_z}}^{t_{j_z}} \end{bmatrix} \begin{bmatrix} C_{\text{ap}} \\ C_{\text{ad}} \\ \frac{1}{R_a} \end{bmatrix} = \begin{bmatrix} \left(\frac{a}{3} \cdot \min(t_{j_1}, T_s)^3 + \frac{b}{2} \cdot \min(t_{j_1}, T_s)^2 \right) - \left(\frac{a}{3} \cdot \min(t_{i_1}, T_s)^3 + \frac{b}{2} \cdot \min(t_{i_1}, T_s)^2 \right) \\ \cdot \\ \left(\frac{a}{3} \cdot \min(t_{j_n}, T_s)^3 + \frac{b}{2} \cdot \min(t_{j_n}, T_s)^2 \right) - \left(\frac{a}{3} \cdot \min(t_{i_n}, T_s)^3 + \frac{b}{2} \cdot \min(t_{i_n}, T_s)^2 \right) \\ \cdot \\ \left(\frac{a}{3} \cdot \min(t_{j_z}, T_s)^3 + \frac{b}{2} \cdot \min(t_{j_z}, T_s)^2 \right) - \left(\frac{a}{3} \cdot \min(t_{i_z}, T_s)^3 + \frac{b}{2} \cdot \min(t_{i_z}, T_s)^2 \right) \end{bmatrix} \quad (4.28)$$

The choice of (t_i, t_j) pairs has great impact on the accuracy of the parameter estimates. If the row vector corresponding to the n^{th} pair is a multiple of the row vector corresponding to the m^{th} pair with different right hand terms, then the LS estimates become ill-conditioned. Thus, it is important to select a set of pairs which minimizes the condition number of the sensitivity matrix.

By setting the weak parameters \widehat{C}_{ap} , \widehat{C}_{ad} , and \widehat{L} at some nominal values, we introduce bias in the model and thus estimates of R_a and Q_{\max} are influenced by how close the weak parameters are to the optimal values: C_{ap}^* , C_{ad}^* , and L^* . We will next highlight the importance of the initial guesses for R_a and Q_{\max} .

4.3.3 Initial guesses of R_a and Q_{\max}

We showed in Section 4.2.2 that the NLLS solution is attained through a sequence of parameter updates. The starting value for each parameter plays an important role in guaranteeing convergence of the algorithm. For each cycle k , we use the NLLS estimate from the previous cycle, $\widehat{\theta}_\rho^{k-1}$, as the initial guess for the reduced parameter vector θ_ρ . Specifically,

$$R_a^{k;i=0} = \widehat{R}_a^{k-1} \quad \text{and} \quad Q_{\max}^{k;i=0} = \widehat{Q}_{\max}^{k-1} \quad (4.29)$$

where i stands for iteration number and k indicates the beat number. This setup requires prior knowledge of the arterial resistance, $R_a^{k=1;i=0}$, and maximum flow, $Q_{\max}^{k=1;i=0}$, at the first beat. Since we use a measurement or estimate of CO from the first beat to determine nominal values for the weak parameters, we could infer $R_a^{k=1;i=0}$ from the steady state equation of the modified Windkessel model in the first beat: $R_a^{k=1} = \frac{\text{MAP}_1}{\text{CO}_1}$. An initial guess of maximum flow, $Q_{\max}^{k=1;i=0}$, is determined using

the analytical expression of blood flow when modeled as a parabolic pulse train: $Q_{\max}^{k=1} = \frac{3}{2}\beta_1 CO_1$.

4.3.4 Summary diagram

The overall behavior of our beat-by-beat estimation algorithm can be summarized in the following steps:

1. Detect the onset of each cycle in measured $P_{ap}(t)$ and $P_{ad}(t)$.
2. Construct P_{measured} as defined in Eq. 4.6 and extract cycle characteristics such as mean arterial pressure, MAP_k , and the beat duration, T_k .
3. Determine the initial conditions for $\hat{P}_{ap}(t_0)$, $\hat{p}_{ad}(t_0)$, and $\hat{I}_l(t_0)$.
4. Optimize using a grid search for the weak parameters \hat{L} , \hat{C}_{ap} , and \hat{C}_{ad} to reduce the estimation bias.
5. Run the NLLS on each cycle sequentially to estimate R_a and Q_{\max} in each cycle. Set $\hat{\theta}_\rho$ to the parameter vector with the smallest RMSE for each cycle.

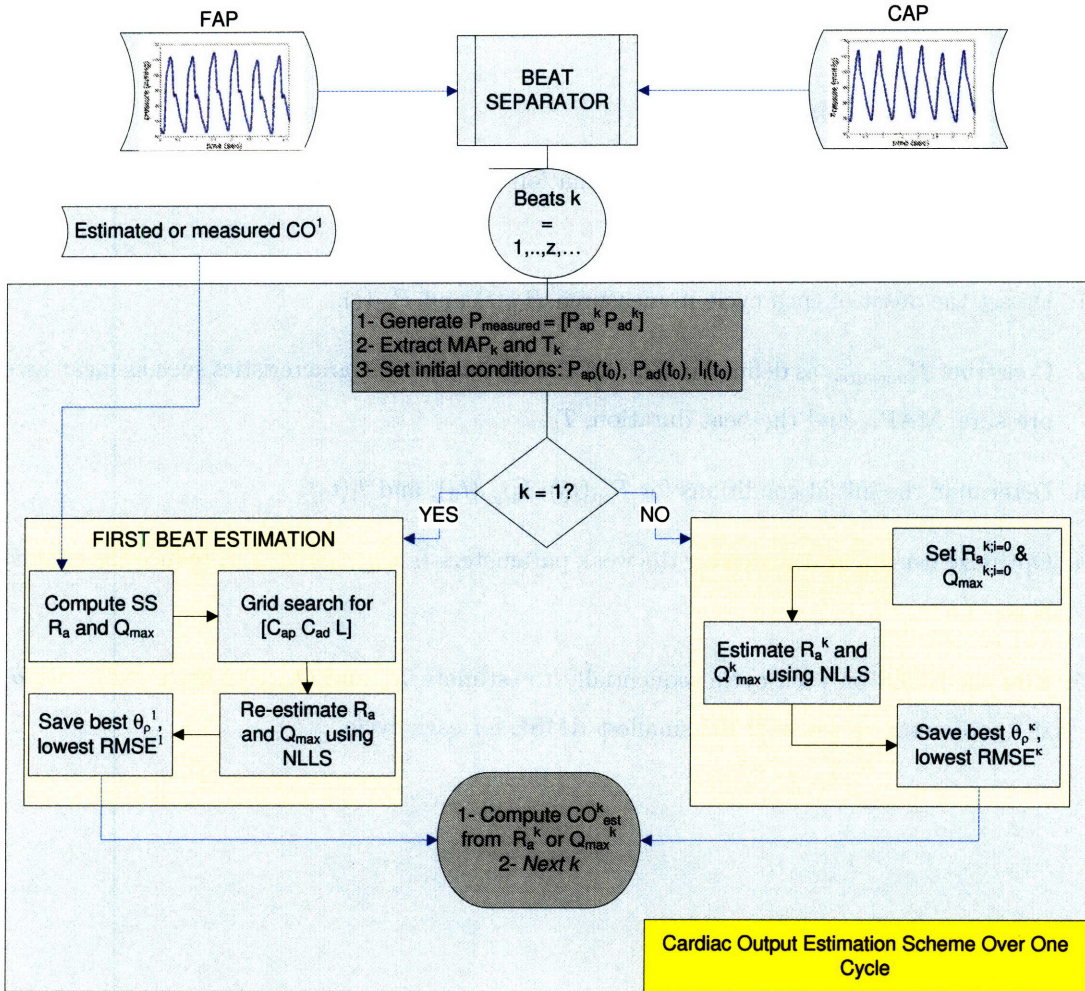


Figure 4-4: Beat-by-beat parameter estimation algorithm. Inputs FAP and CAP stand for fABP and cABP respectively.

4.4 Concluding Remarks

In this chapter, we described in detail our estimation scheme. We applied standard NLLS estimation techniques by taking advantage of all the degrees of freedom of the Levenberg-Marquardt algorithm, the weighted residuals, and the scaled Jacobian. We then highlighted the mechanics of a beat-by-beat estimation algorithm which is intended to be integrated in ICU monitoring systems. In the following chapter, we apply our estimation scheme to data recorded from four pigs. We validate the estimates of cardiac output and arterial resistance by comparing them to the true CO derived from measured blood flow, $Q(t)$.

Chapter 5

Results

We validated our beat-to-beat estimation algorithm described in Chapter 4 on a porcine data set collected at MIT in a study by Professor Mukkamala of Michigan State University [12]. High resolution pressure and blood flow waveforms as well as electrocardiogram recordings of six Yorkshire swine (30 – 34kg) were recorded for each animal. A micromanometer-tipped catheter was used to measure central aortic pressure and an external pressure transducer was placed to monitor femoral artery pressure. Reference cardiac output, which we refer to as *true CO* although it contains some measurement noise, was obtained using a flow probe placed around the aortic root. This data set has been extensively scrutinized by Parlkar *et al.* [19] and Mukkamala *et al.* [12] for CO estimation. The following cardiovascular variables were recorded for all six swine:

1. Pressure waveforms: central aortic pressure (*cABP*), femoral artery pressure (*fABP*), radial artery pressure (*rABP*).
2. Heart rate (HR), from electrocardiography recordings (ECG) or from pressure waveforms.
3. Blood flow, $Q(t)$.
4. Time stamps for the IV medication infusions, such as esmolol, phenylephrine, nitroglycerine, and dobutamine.

5.1 Description of the Porcine Data

The experiments by Professor Mukkamala aimed to identify the effects of numerous drugs such as dobutamine, nitroglycerine, esmolol, and phenylephrine on CO, HR, and ABP [12]. The porcine data set contains hemodynamic states spanning a wide dynamic range. Figure 5-1 shows some of the recordings corresponding to Pig #6. We see that the administered drugs lead to high variability in cardiac output, heart rate and mean arterial pressure. For instance, dobutamine, which is known

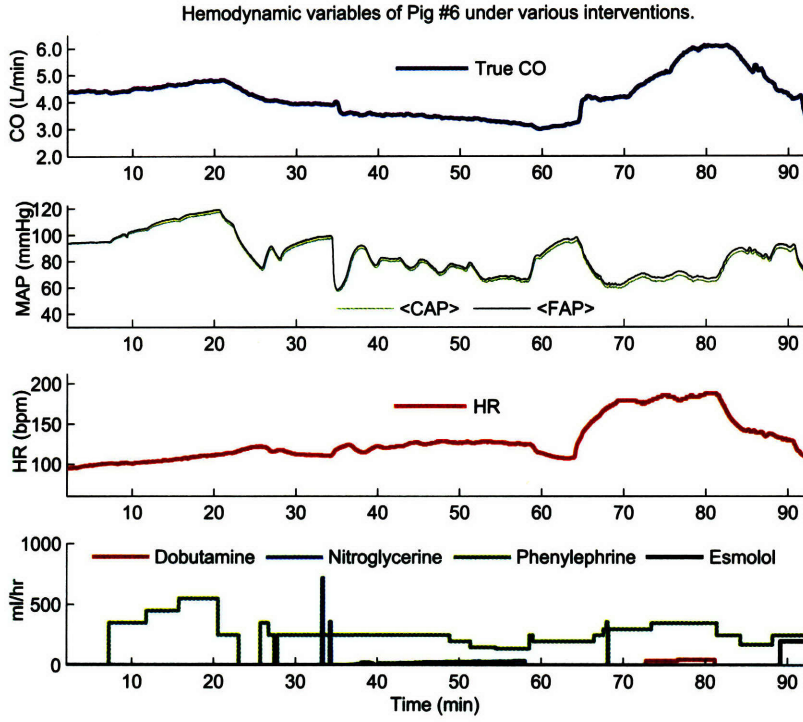


Figure 5-1: Typical recordings from the study by Dr. Mukkamala *et al.* [12]. These waveforms correspond to Pig #6. Note that we show mean arterial pressure of central aortic pressure and femoral artery pressure rather than the measured waveforms.

for its effect on cardiac output and contractility, leads to an increase in cardiac output minutes after its injection at $t = 73$ min. Once it was turned off 7 minutes later, cardiac output decreases. The injection of nitroglycerine at $t = 34$ min caused the blood pressure to drastically decrease and heart rate to increase slightly without affecting cardiac output. Esmolol which is used in clinical settings to prevent tachycardia, was administered at $t = 88$ min and caused the heart rate to decrease. The effect of phenylephrine, which was administered with different levels throughout the recording time, is greatest at $t = 58$ min: blood pressure increased with the higher level of phenylephrine. Also, at $t = 20$ min, a reduction in the level of phenylephrine lead to a significant decrease in mean blood pressure.

5.2 One-Cycle Fitting

In Chapter 2, the modified Windkessel model was shown to be a valid model of the arterial tree, from the left ventricle to a distal artery. In Chapter 4, we described a grid search over physiological ranges for C_{ad} , C_{ap} , and L to reduce the bias resulting from fixing the weak parameters so as to obtain best fits to the measured data for a given CO. We further discussed an iterative NLLS estimation

algorithm to compute beat-by-beat estimates for R_a and Q_{\max} for some fixed values of C_{ad} , C_{ap} , and L .

Figure 5-2 shows how the estimation algorithm generates well-behaved pressure cycles that match the measured data. The algorithm in this case minimizes the RMSE over a certain number of iterations to obtain parameter estimates for one cycle. The underlying parameters of the modeled waveforms corresponding to the smallest *RMSE* are considered to be good estimates of the true values of arterial resistance and maximum flow for the k^{th} cycle, and are then used to compute cardiac output in the k^{th} cycle, CO_k .

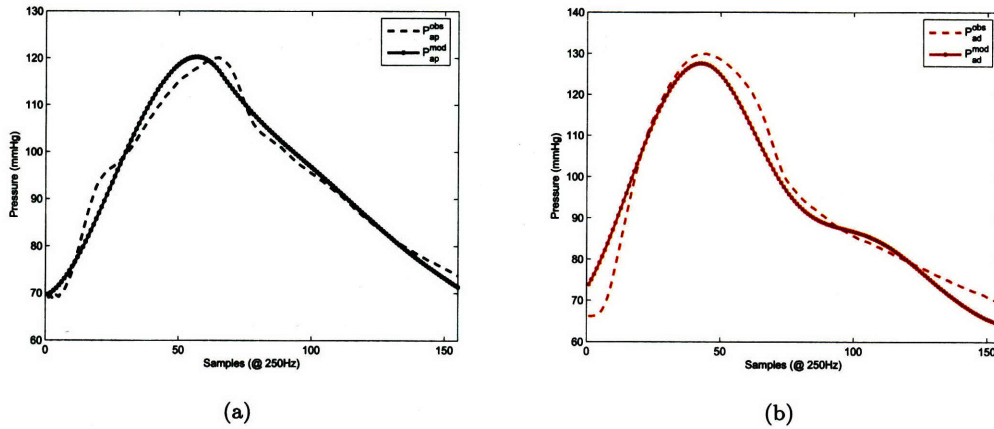


Figure 5-2: Fits to the 11th pressure cycle from pig #6 after 8 iterations: a) central aortic pressure b) femoral artery pressure.

5.3 Continuous Monitoring of Four Pigs

Although the data set contains recordings of six pigs, we apply our estimation algorithm only to four pigs as pig #4 and pig #7 have noisy central pressure waveforms. The resulting CO estimates were evaluated using a normalized version of the root mean squared error. The *root-mean-squared-normalized-error*, RMSNE, as suggested by its name, normalizes the cardiac output prediction errors by the true value so as to obtain a unitless measure of prediction error. For a given pig, the RMSNE is as follows:

$$\text{RMSNE} = 100 \times \sqrt{\frac{1}{N_{\text{co}}} \sum_{i=1}^{N_{\text{co}}} \left(\frac{\text{CO}_{\text{est}}^{(i)} - \text{CO}_{\text{true}}^{(i)}}{\text{CO}_{\text{true}}^{(i)}} \right)^2} \quad (5.1)$$

where N_{co} is the number of cardiac output measurements for a given pig. In Table 5.1, we report the resulting RMSNE for all four pigs in two forms: RMSNE_{unfiltered} represents the overall root mean squared normalized error between the raw CO estimates and the true CO. RMSNE_{filtered} takes into account the smoothing of CO estimates using a median filter of width 40 beats. We also show the RMSNE as reported by Parlkar *et al.* [19] and the number of beats used in their estimation scheme.

Pig #	Number of beats	RMSNE _{unfiltered}	RMSNE _{filtered}	Number of beats	RMSNE _{Parlikar}
5	13234	12.1%	9.8%	14404	10.8%
6	11538	19.2%	18.6%	12088	9.4 %
8	13020	12.2%	11.1%	14113	12.6%
9	7717	19.6%	18.6%	9370	19.6%

Table 5.1: Estimation algorithm performance evaluation and comparison with the results by Parlikar *et al.* [19] using RMSNE for the four pigs.

As can be seen in Table 5.1, the RMSNE can be as low as 9.8% and as high as 19.6%, as seen in pig #9. To justify the wide range of RMSNE, we looked at the intra-beat dynamics in pig #9 and pig #5. The difference in estimation precision can be attributed to the reflections observed in the proximal pressure waveform of pig #9 during systole. In our estimation algorithm, we align the peaks of the pressure cycle generated by the modified Windkessel model and that of the measured cycle. For beats with type A reflections, there are two local maxima in systole which could cause the misalignment of the beats and ultimately affects the quality of the R_a and Q_{max} estimates.

Although the RMSNE provides us with an overall measure of the algorithm's performance, it is important to examine the reliability of the algorithm under various hemodynamic conditions. Figures 5-3, 5-4, 5-5, and 5-6 show CO, R_a , MAP and HR as a function of time. Note that throughout the experiments, the pigs were infused with drugs to cause the observed dynamics.

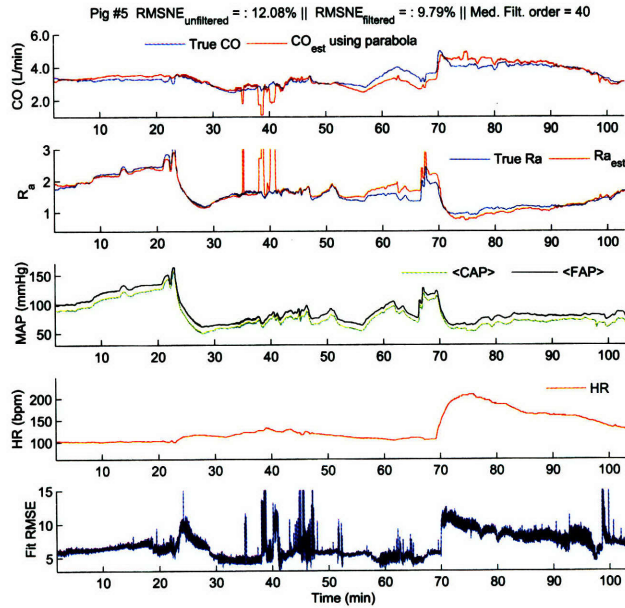


Figure 5-3: Pig #5 cardiac output and arterial resistance estimates as a function of time. The goodness-of-fit of the pressure waveforms is reported in the bottom window.

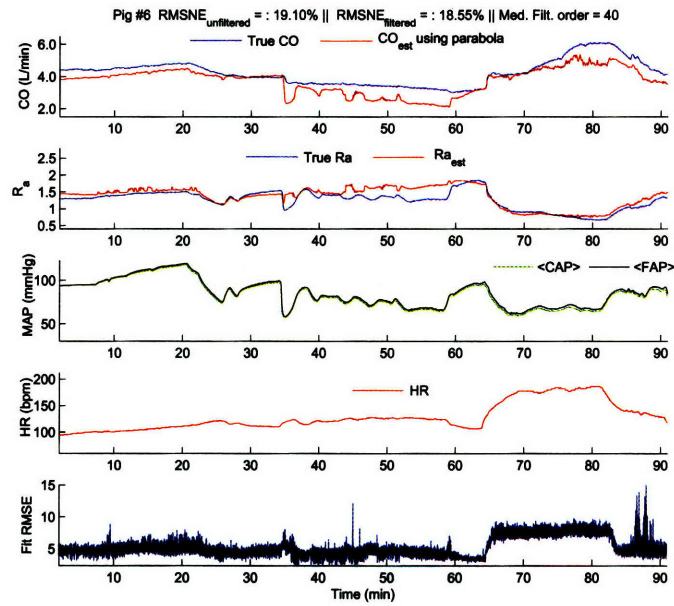


Figure 5-4: Pig #6 cardiac output and arterial resistance estimates as a function of time. The goodness-of-fit of the pressure waveforms is reported in the bottom window.

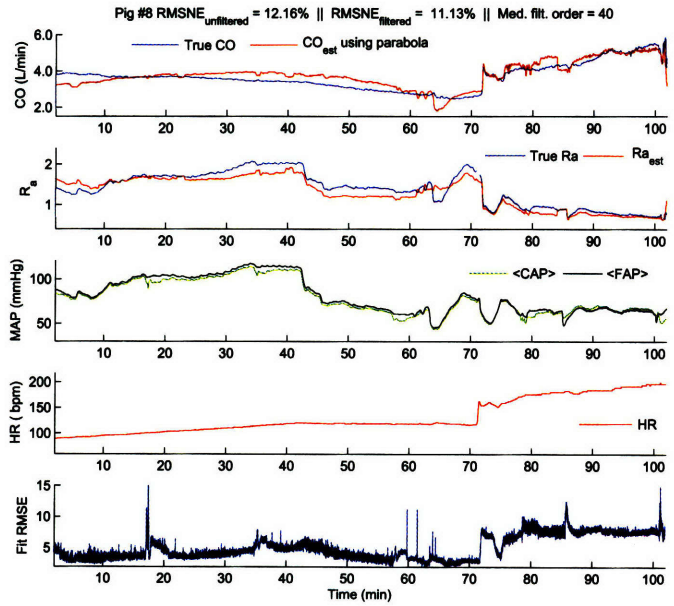


Figure 5-5: Pig #8 cardiac output and arterial resistance estimates as a function of time. The goodness-of-fit of the pressure waveforms is reported in the bottom window.

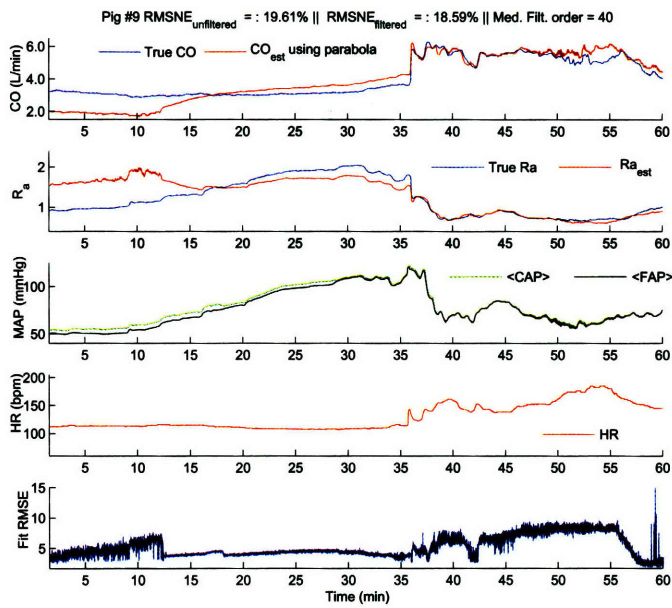


Figure 5-6: Pig #9 cardiac output and arterial resistance estimates as a function of time. The goodness-of-fit of the pressure waveforms is reported in the bottom window.

Remarks: We previously explained the lower precision in the cardiac output estimates for pig #9 as opposed to that for pig #5, attributing the imprecise estimates to the reflections observed in the central aortic pressure waveform. This hypothesis however is not the only justification for the high RMSNE. By looking at Figure 5-6, one can see that the CO estimates after $t = 15$ min are very close to the true values, however, during the first 15 minutes, the estimates are almost off by 1 L/min. Also, notice that pig #9 was initially hypotensive. Further investigation of the dependency of estimation error and mean arterial pressure reveals that there exists a correlation between the level of MAP and the prediction error as can be seen in Figure 5-7. The number of samples corresponding to low MAP is larger than that for high MAP, however, it is fair to conclude that for low MAP, the variance of the estimation error is larger than the variance for high MAP, and that the estimation algorithm is more likely to underestimate cardiac output as the mean of the prediction error is negatively biased.

The prediction error is not the only indication that the estimation algorithm is not as accurate for low MAP as for normal or high MAP. The bottom plot in Figures 5-3, 5-4, 5-5, and 5-6 show the fit RMSE between the pressure cycle generated by the modified Windkessel model and the measured pressure waveforms. We observed that for low MAP, the fit RMSE is higher than that in the normal and hypertensive cases. This dependency of the estimates accuracy on MAP can be justified by the relationship between arterial compliance and pulse pressure. In Chapter 3, we indicated that compliance is a pressure-dependent parameter which is highly correlated with pulse pressure: for a given stroke volume, when pulse pressure decreases arterial compliance is expected to increase. However in our estimation algorithm, we hold both C_{ap} and C_{ad} constant. Under the assumption that compliance is equal to the ratio of stroke volume to aortic pulse pressure, Eq. 3.12 states that pulse pressure scales with MAP, and consequently, compliance should be dynamically adjusted throughout the estimation process.

5.4 Statistical Significance of Estimated Parameters

In the previous section we evaluated the performance of the estimation algorithm for each of the pigs. We now attempt to describe the aggregate performance of the algorithm by first determining the aggregate RMSNE over all four pigs, followed by the Bland-Altman plot using all estimated cardiac output values.

Aggregate RMSNE: The aggregate RMSNE for all four pigs combined is about 13.8% using 45509 CO samples. The estimation error has a mean equal to -0.094 L/min and a standard deviation of 0.486 L/min.

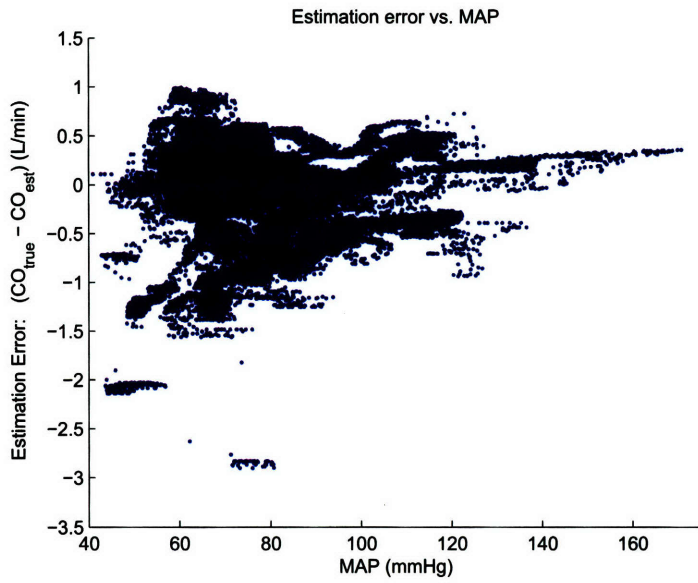


Figure 5-7: CO estimation error as a function of the mean arterial pressure. The higher the MAP, the larger the CO estimation error. The correlation, r_2 , between MAP and the Estimation error is 0.19

Linear regression: Figure 5-8 superimposes the equality line, on a scatter plot of CO_{est} and CO_{true} . It can be seen that most samples lie along the direction of the $\text{CO}_{\text{est}} = \text{CO}_{\text{true}}$ line which suggests that the estimates obtained from the modified Windkessel model agree with the measured values. The correlation coefficient, r , between CO_{est} and CO_{true} is equal to 0.87 ($p < 0.001$).

Bland-Altman plot [57]: In order to assess the agreement between CO_{est} and CO_{true} , we generate the Bland-Altman plot, an extensively used method in clinical research for the comparison between different methods of measuring some physiological quantity [57]. The Bland-Altman plot in Figure 5-9 shows the correspondence between the estimation error and the average of the values from the two methods. It can be seen that most of the estimates lie within ± 0.960 L/min, which allows us to claim that our estimation algorithm is a good alternative to the aortic flow probe.

5.5 Limitations

1. The precision of the cardiac output estimates comes with a computational cost which could be met using more powerful computers. On average, the expected running time of the estimation algorithm is six times longer than the actual duration of the waveform. We ran the estimation algorithm on a Pentium 4 machine (3.4 GHz, 1.00 GB of RAM). The current high computational cost does not allow us to use the estimation algorithm as an online estimation scheme in ICUs.

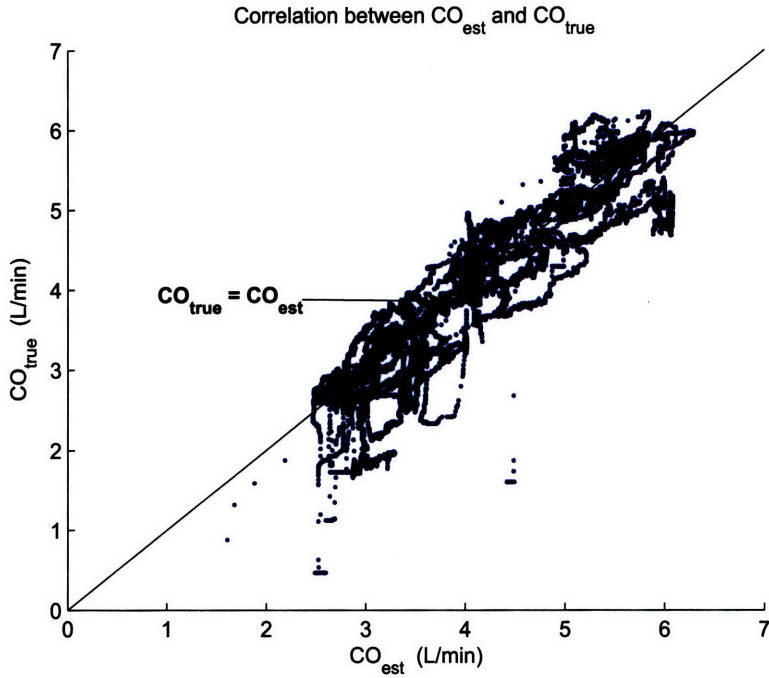


Figure 5-8: Linear regression plot for cardiac output estimates for 45,509 beats.

2. The algorithm requires a cardiac output measurement for the first cycle in order to set the weak parameters at some fixed value.
3. We hold pressure-dependent parameters at fixed values. We previously observed in Section 5.3 that the prediction error and the resulting fits are worse when MAP is low as we do not dynamically adjust the arterial compliances.

5.6 Concluding Remarks

We applied the estimation algorithm to four pigs in various hemodynamic states. We obtained reliable estimates of cardiac output and arterial resistance with high confidence: the aggregate RMSNE over the four pigs was 13.8%. The Bland-Altman plot suggests that the invasive flow measurement for determining cardiac output can be interchanged with our estimation algorithm. However, given the current method, it may be too computationally expensive to perform the estimation on a beat-by-beat basis.

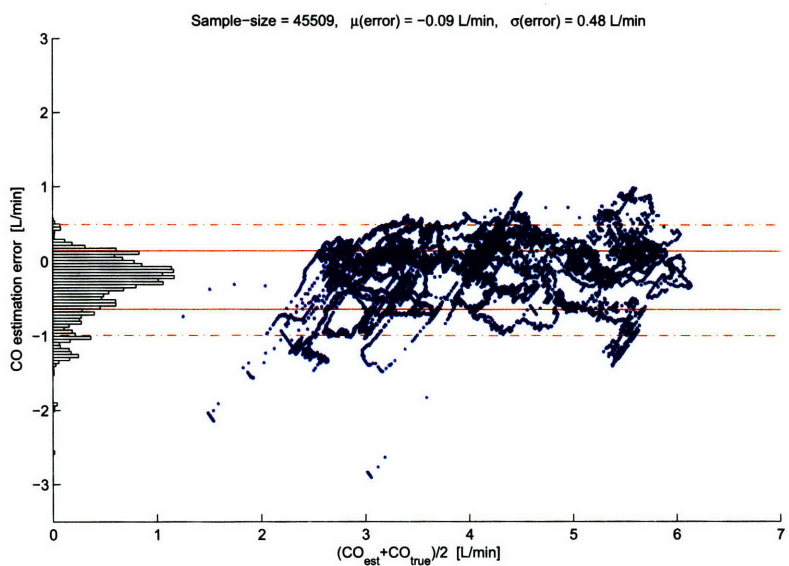


Figure 5-9: Bland-Altman plot for cardiac output estimates over 45,509 porcine cycles. The solid red lines define the 1-SD error, and the dashed red lines determine the 2-SD error.

Chapter 6

Conclusions and Future Work

In this thesis, we presented an ambitious attempt to estimate cardiac output and arterial resistance from measurements of blood pressure using the modified Windkessel model. Our approach was twofold: we first analyzed in detail the modified Windkessel model and its parameter space before investigating the inverse problem of estimating cardiac output and arterial resistance using pressure waveforms. In this chapter, we provide a summary of the thesis document followed by suggestions for future work.

6.1 Summary

Chapter 2 addressed the limitations of the two-element Windkessel model and presented two higher order variations: the three-element Windkessel model and the modified Windkessel model. We qualitatively validated the modified Windkessel model as a good representation of the arterial tree in both the time and the frequency domain. We further explored various pulse shapes for modeling the blood outflow at the left ventricle. We observed that a parabolic pulse train provided good fits to flow waveforms and resulted in well-behaved proximal and distal pressure waveforms. We concluded Chapter 2 with a comparison of the two-element Windkessel model and the modified Windkessel model in the frequency domain. We suggested that at low frequencies, the two-element Windkessel model is equivalent to the modified Windkessel model, however, the equivalence does not hold at high frequencies.

Chapter 3 presented a detailed analysis of the parameter space of the modified Windkessel model. Sensitivity analysis was first conducted to determine the effect of each parameter on the proximal and distal pressures. Given that the Hessian matrix was ill-conditioned, a subset selection method was applied to our parameter space to determine which parameters could be estimated accurately. Parameters R_a , Q_{\max} and L were then chosen as strong parameters which could be well identified using least squares techniques, while C_{ad} , C_{ap} and P_v were considered weak parameters.

We further simplified the parameter vector to contain R_a and Q_{\max} only since their variations are much faster than the variations in blood inertance, L . We then addressed the issue of setting the weak parameters by first summarizing previous approaches developed by other researchers to estimate arterial compliance and blood inertance.

Chapter 4 focused on the details of the inverse problem: estimating cardiac output and arterial resistance from measurements of blood pressure waveforms. We first turned our attention to the nonlinear dependency of pressure waveforms on the parameters, R_a and Q_{\max} . We then presented the Gauss-Newton approximation to the Hessian to derive a nonlinear version of the least squares method. The Levenberg-Marquardt regularization algorithm was then discussed as a possible regularization technique to stabilize the iterative estimation process. Finally, we described our beat-by-beat estimation algorithm, including the details of setting up the initial conditions for the state variables in the model and the best initial guesses for all six parameters.

Chapter 5 illustrated the validity of the our estimation algorithm using porcine data. We first described the data set under investigation before reporting the performance of our estimation algorithm on each of the pigs. We obtained promising results under various hemodynamic conditions. The limitations of our estimation algorithm were then laid out.

6.2 Suggested Improvements to the CO Estimation Algorithm

In Chapter 5, we listed some of the limitations of our estimation scheme. Bypassing these limitations could result in substantial improvement of the accuracy of the computed estimates and consequently, our estimation method would yield reliable assessment of cardiac output. We will explore three possible adjustments to the algorithm.

Beat-by-beat compliance estimation: In Chapter 3, we presented a detailed summary of methods developed by other researchers to estimate either total arterial compliance in the two-element Windkessel model or the three-element Windkessel, or the proximal and distal compliances in the modified Windkessel model. Some methods assumed a nonlinear pressure-volume relationship which lead to a pressure-dependent compliance. In Chapter 5, we saw that one of the limitations of our estimation algorithm is that it does not adjust the arterial compliances with variations in MAP. Such an improvement could result in much better cycle fits and cardiac output estimates in low pressure conditions.

Online estimation: In Chapter 5, we discussed the computational limitation of our estimation algorithm which hinders the applicability of our method in the ICU. Given that the current gold

standard consists of intermittent measurements of cardiac output via thermodilution, we could modify our estimation scheme so that it estimates cardiac output and arterial resistance every tenth beat. Consequently, the estimation algorithm will resemble any other online method for the estimation of cardiac output. An additional step could be taken to reduce the noise within the cycle, namely, to average every 10 beats so that the target beats resemble the pressure waveforms generated by the modified Windkessel model. During transients, a beat-by-beat estimates should be obtained.

Estimating $\beta = \frac{T_k}{T_s}$: For human subjects, we set $\beta = 3\sqrt{T_k}$. However, this relationship does not hold for porcine data, $\frac{T_k}{T_s} \approx 2.4$. For the validation of our estimation scheme on porcine data, we fixed β at 2.4. The sensitivity of the pressure waveforms to β could justify some of the high errors observed in the waveform fit RMSE which we could minimize by dynamically adjusting β based on heart rate. Further studies of flow waveforms are needed to determine relationships between heart rate and β .

6.3 Plausible Extensions

In addition to the improvements to our estimation algorithm, we also suggest some promising research explorations.

Applying the estimation algorithm to human data: Our estimation algorithm performed well on porcine data but we ultimately would like to provide an alternative to thermodilution in the ICU, which requires extensive application to human data. The MIMIC II database [24] contains all necessary inputs to our estimation algorithm. Given that intermittent measurements of cardiac output were taken using thermodilution, we could validate the resulting beat-by-beat estimates of cardiac output to that obtained using the two-element Windkessel in Parlikar *et al.* [19].

Frequency domain analysis: We saw in Chapter 2 that the modified Windkessel model has the same frequency response over low frequencies as the two-element Windkessel model. Over low frequencies, the total arterial compliance, C_a , in the two-element Windkessel is approximately equal to the sum of the two compliance, C_{ad} and C_{ap} . The above observation motivates the implementation of a cascaded estimation scheme in which we first estimate the parameters of the two-element Windkessel based on Parlikar and coworkers method in [19] and then we estimate the parameters of the modified Windkessel model: L , C_{ad} and C_{ap} .

Signal quality index: Our estimation algorithm relies on the information embedded in the intra-beat dynamics of each cycle. Hence, if the morphology of the pressure cycle is distorted either by

wave reflections or by external disturbance to the transducer, we cannot expect to obtain accurate estimates of CO. It is therefore beneficial to compute a signal quality index which will determine whether the pressure waveforms we use are to be trusted or not. Such an approach has been adopted by Sun [13] who developed a signal quality index as a pre-processing step CO estimation algorithms.

Bibliography

- [1] The Leapfrog Group, ICU physician staffing fact sheet, <http://www.leapfroggroup.org/>.
- [2] C.W. Hanson, C.S. Deutschman, H.L. Anderson, P.M. Reilly, E.C. Behringer, C.W. Schwab and J. Price, "Effects of an organized critical care service on outcomes and resource utilization: A cohort study", *Critical Care Medicine*, vol. 27, no. 1, pp. 270-274, February 1999.
- [3] N. Westerhof, N. Stergiopoulos and M. I. M. Noble, *Snapshots of hemodynamics: an aid for clinical research and graduate education*, New York: Springer, 2005.
- [4] O. Frank, "Die Grundform des arteriellen Pulses erste Abhandlung: mathematische Analyse", *Z. Biol.*, vol. 37, pp. 483-526, 1899.
- [5] T.G. Coleman, "Mathematical analysis of cardiovascular function," *IEEE Transactions on Biomedical Engineering*, vol.32, pp. 289-294, April 1985.
- [6] M.P. Spencer and A.B. Denison, "Pulsatile blood flow in the vascular system," in *Handbook of Physiology*, vol. 11, No. 2, chapter 25, Washington, DC: American Physiological Society, 1963.
- [7] G. Liljestrand and E. Zander, "Vergleichende bestimmungen des minutenvolumens des herzens beim menschen mittels der stickoxydulmethode und durch blutdruckmessung," *Research in Experimental Medicine*, vol. 59, pp. 105-122, 1928.
- [8] J.W. Clark Jr., R.Y.S. Ling, R. Srinivasan, J.S. Cole, and R.C. Pruett, "A two-stage identification scheme for the determination of the parameters of a model of left heart and systemic circulation," *IEEE Transactions on Biomedical Engineering*, vol. 27, no. 1, pp. 20-29, January 1980.
- [9] M. Guarini, J. Urza, A. Cipriano and W. Gonzalez, "Estimation of cardiac function from computer analysis of the arterial pressure waveform," *IEEE Transactions on Biomedical Engineering*, vol. 45, no. 12, pp. 1420-1428, December 1998.
- [10] A.T. Reisner, Y. Zhang and H.H. Asada, "Noninvasive cardiac output monitoring based on multi-channel blind system ID and modal decomposition," *Proceedings of the Second Joint EMBS/BMES Conference*, October 2002.

- [11] R. Mukkamala, G. Swamy, Q. Ling and T. Li, "Blind identification of the central aortic pressure waveform from multiple peripheral arterial pressure waveforms," *Proceedings of the 28th IEEE EMBS Annual International conference in New York, USA*, September 2006.
- [12] R. Mukkamala, A.T. Reisner, H.M. Hojman, R.G. Mark and R.J. Cohen, "Continuous cardiac output monitoring by peripheral blood pressure waveform analysis," *IEEE Transactions on Biomedical Engineering*, vol. 53, no. 3, pp. 459-467, March 2006.
- [13] J. Sun, "Cardiac output estimation using arterial blood pressure waveforms", *M.Eng. Thesis*, Department of Electrical Engineering and Computer Science, MIT, Cambridge, MA, September 2006.
- [14] C. H. Chen, E. Nevo, B. Fetics, P.H. Pak, F.C.P. Yin, W.L. Maughan, and D.A. Kass, "Estimation of central aortic pressure waveform by mathematical transformation of radial tonometry pressure: validation of generalized transfer function," *Circulation*, vol. 95, pp. 1827-1836, April 1997.
- [15] M. Karamanoglu, M.F. O'Rourke, A.P. Avolio, and R.P. Kelly, "An analysis of the relationship between central aortic and peripheral upper limb pressure waves in man," *Euro. Heart. J.*, vol. 14, no. 2, pp. 160-167, February 1993.
- [16] T. Heldt, J.L. Chang, G.C. Verghese and R. G. Mark, "Cycle-averaged models of cardiovascular dynamics" in *Modelling and Control in Biomedical Systems, 2003*, pp. 387-391, Elsevier, Oxford, UK, 2003.
- [17] M. Burth, G.C. Verghese, and M. Velez-Reyes, "Subset selection for improved parameter estimation in on-line identification of a synchronous generator", *IEEE Transactions on Power Systems*, vol. 14, no. 1, pp. 218-225, March 1999.
- [18] T. Parlikar, T. Heldt and G.C. Verghese, "Cycle-averaged models of cardiovascular dynamics", *IEEE Transactions on Circuits and Systems I*, vol. 53, no. 11, pp. 2459-2468, November 2006.
- [19] T. Parlikar, G.C. Verghese, T. Heldt and G. V. Ranade, "Model-based continuous monitoring of cardiac output and total peripheral resistance.", personal communication.
- [20] K.C. Ehlers, K.C. Mylrea, C.K. Waterson and J.M. Calkins, "Cardiac output measurements. A review of current techniques and research", *Annals of Biomedical Engineering*, vol. 14, no. 3, pp. 219-239, 1986.
- [21] T. Heldt, "Computational models of the cardiovascular response to orthostatic stress", Ph.D. Thesis, Division of Health Sciences and Technology, MIT, Cambridge, MA, September 2004.

- [22] Z. Samar, "Cardiovascular parameter estimation using a computational model", M.S. Thesis, Department of Electrical Engineering and Computer Science, MIT, Cambridge, MA, May 2005.
- [23] Y. Bard, *Nonlinear parameter estimation*, Boston, MA: Academic Press-Harcourt Brace Jovanovich, 1974.
- [24] M. Saeed, C. Lieu, G. Raber, and R.G. Mark, "MIMIC II: a massive temporal ICU patient database to support research in intelligent patient monitoring", *Computer in Cardiology*, vol. 9, pp. 641-644, September 2002.
- [25] P. Segers, P. Verdonck, Y. Deryck, S. Brimioule, R. Naeije, S. Carlier and N. Stergiopoulos, "Pulse pressure method and the area method for the estimation of total arterial compliance in dogs: sensitivity to wave reflection intensity," *Annals of Biomedical Engineering*, vol. 27, pp. 480-485, 1999.
- [26] M.S. Olufsen and A. Nadim, "On deriving lumped models for blood flow and pressure in the systemic arteries," *Mathematical biosciences and engineering*, vol. 1, no. 1, June 2004.
- [27] R.M. Goldwyn and T.B. Watt Jr. "Arterial pressure pulse contour via a mathematical model for the clinical quantification of human vasculature properties," *IEEE Transactions on Biomedical Engineering*, vol.14, pp. 11-17, 1967.
- [28] K.B. Campbell, L.C. Lee, H.F. Frasch and A. Noordergraaf, "Pulse reflection sites and effective length of the arterial system," *American Journal of Physiology* vol. 256, pp. H1684-H1689, 1989.
- [29] N. Westerhof, G. Elzinga and P. Sipkema, "An artificial arterial system for pumping hearts," *Journal of Applied Physiology* Vol.31, no.5, pp. 776-781, 1971.
- [30] P. Segers, I. Coomans, P Verdonck, N. Stergiopoulos, "In vitro evaluation of an extended Pulse Pressure Method for the estimation of total arterial compliance," *Computer in Cardiology*, pp. 153-156, September 1996.
- [31] J.P. Murgo, N. Westerhof, J.P. Giolma and S.A. Altobelli, "Aortic input impedance in normal man: relationship to pressure wave forms," *Circulation*, vol. 62, no.1, pp. 105-116, July 1980.
- [32] M. Bourgeois, B. Gilbert, D. Donald, and E. Wood, "Characteristics of aortic diastolic pressure decay with application to continuous monitoring of changes in peripheral vascular resistance," *Circulation Research*, vol. 35, no. 1, pp. 5666, 1974.
- [33] M. Bourgeois, B. Gilbert, G. Bernuth, and E. Wood, "Continuous determination of beat-to-beat stroke volume from aortic pressure pulses in the dog," *Circulation Research* vol. 39, no. 1, pp. 1524, 1976.

- [34] N. Stergiopoulos, J.J. Meister and N. Westerhof, "Simple and accurate way for estimating total and segmental arterial compliance: the pulse pressure method," *Annals of Biomedical Engineering*, vol. 22, no. 4, pp. 392-297, July 1994.
- [35] P. Segers, N. Stergiopoulos, P. Verdonck, "A non-invasive pulse pressure method for the estimation of total arterial compliance," *Computer in Cardiology*, vol. 24, pp. 171-174, September 1997.
- [36] N. Stergiopoulos, J.J. Meister and N. Westerhof, "Evaluation of methods for estimation of total arterial compliance," *American Journal of Physiology*, vol. 268, pp. H1540-H1540, 1995.
- [37] C.M. Quick, D.S. Berger and A. Noordergraaf, "Apparent arterial compliance," *American Journal of Physiology*, vol. 274, pp. H1393-H1403, 1998.
- [38] D. Chema, J.L. Hébert, C. Coirault, K. Zamani, I. Suard, P. Colin and Y. Lecarpentier "Total arterial compliance estimated by stroke volume-to-aortic pulse pressure ratio in humans," *American Journal of Physiology*, vol. 274, pp. H500-H505, February 1998.
- [39] G.J. Langewouters, L.H. Wesseling and W.J.A. Goedhard "The static elastic properties of 45 human thoracic and 20 abdominal aortas in vitro and the parameters of a new model" *The Journal of Biochemistry*, vol. 17, pp. 425-435, 1984.
- [40] J.W. Remington, C.B. Noback, W.F. Hamilton, and J.J. Gold "Volume elasticity characteristics of the human aorta and the prediction of stroke volume from the pressure pulse," *American Journal of Physiology*, vol. 153, pp. 298-308, 1948.
- [41] H.H. Hardy and R.E. Collins "On the pressure-volume relationship in circulatory elements," *Medical and Biological Engineering and Computing*, vol. 20, no. 5, pp. 565-570, September 1982.
- [42] O.S. Randall, "Effects of arterial compliance on systolic blood pressure and cardiac function" *Clinical and Experimental Hypertension: Theory and Practice*, vol. 7, pp. 1045-1057, 1982.
- [43] R. Burattini, R. Fogliardi and K.B. Campbell "Lumped model of terminal aortic impedance in the dog," *Annals of Biomedical Engineering*, vol. 22, pp. 381-391, July 1994.
- [44] Z. Liu, K. Brin and F. C. P. Yin "Estimation of total arterial compliance: an improved method and evaluation of current methods," *American Journal of Physiology*, vol. 251, pp. H588-H600, 1986.
- [45] N. Westerhof, B.E. Westerhof and N. Stergiopoulos, "Total arterial inertance as the fourth element of the windkessel model", *American Journal of Physiology*, vol. 276, pp. H81-H88, January 1999.

- [46] G.P. Toorop, N. Westerhof and G. Elzinga, "Beat-to-beat estimation of peripheral resistance and arterial compliance during pressure transients" *American Journal of Physiology*, vol. 252, pp. H1275-H1283, 1987.
- [47] T.B. Watt and C.S. Burrus, "Arterial pressure contour analysis for estimating human vascular properties." *Journal of Applied Physiology*, vol. 40, no.1, pp. 171-176, 1976.
- [48] E.R. Rietzschel, E. Boeykens, M.L. De Buyzere, D.A. Duprez and D.L. Clement, "A comparison between systolic and diastolic pulse contour analysis in the evaluation of arterial stiffness," *Hypertension*, vol. 37, pp. 15-22, 2001.
- [49] T.S. Manning, B.E. Shykoff and J. L. Izzo Jr. "Validity and reliability of diastolic pulse contour analysis (Windkessel model) in humans, *Hypertension*, vol. 29, pp. 963-968, 2002.
- [50] P. Segers, A. Qasem, T. De Baker, S. Carlier, P. Verdonck and A. Avolio, "Peripheral 'oscillatory' compliance is associated with aortic augmentation index," *Hypertension*, vol. 37, pp. 1434-1439, 2001.
- [51] K.H. Wesseling, J.R.C. Jansen, J.J. Settels and J.J. Schreuder, "Computation of aortic flow from pressure in humans using a nonlinear, three-element model," *Journal of Applied Physiology*, vol. 74, no. 5, pp. 2566-2573, 1993.
- [52] W.K. Laskey, H.G. Parker, V. A. Ferrari, W.G. Kussmaul and A. Noordergraaf, "Estimation of total systemic arterial compliance in humans," *Journal of Applied Physiology*, vol. 69, no. 1, pp. 112-119, 1990.
- [53] R. Fogliardi, R. Burattini, S.G. Shroff and K.B. Campbell, "Fit to diastolic arterial pressure by third-order lumped model yields unreliable estimates of arterial compliance," *Medical Engineering and Physics*, vol. 18, no. 3, pp. 225-233, April 1996.
- [54] N. Stergiopoulos, J.J Meister and N. Westerhof, "Evaluation of methods for estimation of total arterial compliance," *American Journal of Physiology*, vol. 268, pp. H1540-H1548, 1995.
- [55] Y. Shim, A. Pasipoularides, C.A. Straley, T.G. Hampton, P. F. Soto, C.H. Owen, J.W. Davis and D.D. Glower, "Arterial Windkessel parameter estimation: a new time-domain method," *Annals of Biomedical Engineering*, vol 22, pp. 66-77, 1994.
- [56] J. W. Wolberg and J. R. Berlin, *Data analysis using the method of least squares : extracting the most information from experiments*, New York: Springer, 2006.
- [57] J. Bland and D. Altman, "Statistical methods for assessing agreement between two methods of clinical measurement", *The Lancet*, vol. i, pp. 307-310, 1986.